PLASMA FLOW

Investigation of High Enthalpy Plasma Flow

Damien Le Quang

Aeronautics and Aerospace Department, von Karman Institute for Fluid Dynamics, Belgium, lequang@vki.ac.be

Supervisor: Olivier Chazot

Associate Professor, Head, Aeronautics and Aerospace Department, von Karman Institute for Fluid Dynamics, Belgium, chazot@vki.ac.be

Co-Supervisor: Yacine Babou

Research Engineer, Aeronautics and Aerospace Department, von Karman Institute for Fluid Dynamics, Belgium, babou@vki.ac.be

University Supervisor: Pascal André

Professor, Electric arc and thermal plasmas, France, Pascal.ANDRE@univ-bpclermont.fr

Abstract

A preliminary study of a supersonic air plasma jet produced in the VKI Plasmatron facility is presented. Plasma flow regimes corresponding to underexpanded and highly underexpanded situations are investigated by means of high speed camera imaging. Plasma characterization is performed using Optical Emission Spectroscopy (OES) technique. Several diagnostics allowing to evidence possible departure from thermodynamic equilibrium are presented. OES is performed on both molecular and atomic radiative contribution at the exit of the sonic throat of the convergent nozzle in the first expansion zone. Additionally to the investigation on supersonic air plasma jet, atmospheric pressure plasma jet produced in the Microwave Plasma Torch (MPT) facility is investigated. Using forwarded and reflected microwave power monitoring, electrical characterization of the torch is performed. Simultaneously, comprehensive characterization of the flow by means of high speed imaging evidences the effect of the oscillation of the delivered power on the plasma jet unsteadiness. Basic OES is performed to obtain air, N_2 and CO_2 typical radiative signature.

Keywords: Plasma, Optical Emission Spectroscopy

1. Introduction

During hypersonic atmospheric entries, the radiative heating experienced by a vehicle is a major issue for accurate prediction of thermal heat flux. Computational tools development requires experimental data to assess the the reliability of models. In particular, non equilibrium kinetic models need to be assessed in order to replicate the radiative contribution of the excited gas in the shock layer where collisional and radiative processes lead to thermodynamic non equilibrium situations. Due to the relatively large cost of missions and the difficulty of performing accurate measurements in flight, plasma source ground test facilities have been developed. The most common devices allowing electrodeless operations are the RF inductively coupled and microwave plasma sources where the discharge is ignited and sustained by high-frequency electromagnetic fields. In this study, experimental studies were carried out using the Plasmatron Inductively Coupled Plasma (ICP) and Microwave Plasma Torch (MPT) VKI facilities. Concerning the Plasmatron facility, the study is focused on the interpretation of spectroscopic measurements performed in the first expansion zone of a supersonic underexpanded air plasma jet. A sonic throat has been installed on VKI Plasmatron facility to obtain a strong expansion. In the literature, the use of supersonic plasma jets to investigate non equilibrium processes has been widely reported but most investigations deal with mono-atomic gases (Sember & al.[1], Selezneva & al.[2] and Sanden & al. [3]). Robin

& al.[4] have investigated a supersonic nitrogen arc plasma jet to examine the kinetic scheme of ionic recombination. Various technologies are used to obtain supersonic plasma jets. Yano & al. [5] have developed a facility to generate a supersonic high pressure glow discharge. High speed plasma flow can be generated from a magnetic nozzle [6] that reduces power losses occurring in solid nozzles. In our study, the expansion of the plasma is performed through a sonic throat into a low pressure chamber. In a such flow, the expansion of the plasma is accompanied by a rapid cooling and recombination which results in kinetic non equilibrium between electrons and heavy particles. In this situation, the plasma is recombining by collisional processes and a departure from Saha-Boltzmann equilibrium is observed. Non intrusive method based on Optical Emission Spectroscopy (OES) are commonly used to characterize supersonic plasma jets. They allow to get excited level densities of various species. Although OES studies are encouraged in supersonic plasma jets, characterization have to be carried using cautious assumptions. Sember & al. [1] have shown that spectroscopic analysis based on atomic lines, and hydrogen lineshape profiles might give questionable results if the plasma is out of thermodynamic equilibrium. In this study, proper diagnostics based on atomic and molecular contributions have been developed to evidence the non equilibrium state.

A detailed investigation of the plasma source performance is necessary to insure high quality measurements. Frequency analysis of electrical parameters and light emission are the most common ways to understand the nature of the plasma jet fluctuations. In the literature, much effort is devoted to the diagnostic of the arc plasma jet unsteadiness (Tu al. ([7]), Singh & al [8]). In RF plasma sources, the heating procedure may also induce oscillations in the emission. Performance of the Microwave Plasma Torch (MPT) producing atmospheric plasma is investigated. Electrical characterization of the source has been performed for some operating conditions using forwarded and reflected microwave power monitoring. Comprehensive characterization of the flow by means of high speed imaging has been performed to estimate the effect of the oscillation of the delivered power on plasma jet unsteadiness. Basic OES measurements are performed to get typical radiative signatures of air, N_2 and CO_2 atmospheric plasma jets.

Diagnostics adopted to examine the thermodynamic state present in the Plasmatron supersonic air plasma jet are described in section 2 and the results are presented in section 3. Performances of MPT will be discussed in section 4.

2. Spectroscopic plasma diagnostics

2.1. Plasma diagnostics using atomic lines

2.1.1. Atomic state distribution function

Measured emission ϵ_{ul} allows a straight probing of the upper (emitting) level n_u population density through the relation:

$$\epsilon_{ul} = n_u \frac{A_{ul}}{4\pi} \frac{hc}{\lambda_{ul}} \quad (W.m^{-3}.sr^{-1}), \tag{1}$$

where A_{ul} (s^{-1}) is the Einstein coefficient associated to spontaneous emission from level u to level l respectively of energy E_u and E_l (m^{-1}). $\lambda_{ul} = \frac{1}{(E_u - E_l)}$ (m) designates the line position. Assuming Local Thermodynamic Equilibrium (LTE), the internal level population density of a level u of energy E_u and degeneracy g_u follows the Boltzmann distribution ruled by a single temperature T_{LTE} given by:

$$n_u(T_{LTE}) = N(T_{LTE}) \frac{g_u exp\left(-\frac{hcE_u}{k_B T_{LTE}}\right)}{Q_{int}(T_{LTE})} \quad (m^{-3}), \tag{2}$$

where species concentration N (m^{-3}) and internal partition function Q_{int} are calculated at equilibrium.

In thermal plasmas, atomic state distribution function obeys Boltzmann equilibrium and the excitation temperature T_{exc} is evaluated on the basis of the Boltzmann diagram method. This approach is convenient as no assumption is made concerning the species concentration. The upper level density being straightly related to emission through relation 1, it is expressed in terms of T_{exc} combining equations (1) and (2) in the form:

$$ln\left(\frac{n_u}{g_u}\right) = -\left(\frac{hc}{k_b T ex}\right) E_u + ln\left(\frac{N}{Q_{int}}\right). \tag{3}$$

Excitation temperature T_{exc} is directly obtained from the slope of a straight line fitted on the set of experimental electronic excited states population logarithm values (left term of Equation 3).

Occasionally, the equilibrium distribution is not applicable to electronic states. In this case, experimental points in Boltzmann diagram do not comply with a single straight line. In order to qualitatively express the departure from equilibrium, it is convenient to defined two temperatures T_{exc}^{low} and T_{exc}^{high} corresponding respectively to the excitation temperature of lower and higher states. In such case, it is important to know

if ionizing or recombining state is prevailing in the plasma in order to determine the electron temperature T_e. For this purpose, the atomic state distribution function can be completed using the so-called Saha point n_∞ defined as:

$$\frac{n_\infty}{g_\infty} = \frac{n_2^2}{2g_0^i} \times \left(\frac{h^2}{2\pi m_e k T_e}\right)^{3/2} \quad (4)$$

Where g_0^i is the degeneracy of the ground state of the corresponding ion. In a situation of Partial Local Saha Equilibrium (pLSE), the Saha point will be within the line that fits the levels with populations conforming to the Saha Boltzmann equation. In a first approximation, the ground state n_0 can be evaluated using equation 5. Its position with regard to the pLSE fitted line will determine the pLSE ionizing or recombining state. Such investigation is not presented in the following as it requires missing information on the pressure inside the jet.

$$n_0 = P/kT_{gas} \quad (5)$$

2.1.2. Stark broadening of hydrogen lines

The determination of the electronic number density is executed though the fitting of calculated hydrogen Stark broadened lines onto experimental data. Calculation of the the Stark broadened line profiles have been reported in the literature for the first three Balmer lines of hydrogen (H_α, H_β and H_γ). Databases are elaborated using three different theoretical models named as quasi-static ion approximation model (VCS)[9], Model Microfield Method (MMM)[10] and Computer Simulation (CS)[11]. The available domains for each set of theoretical data are presented in table 1. The line half-profiles are available in the form of tables where values of intensity are tabulated against wavelengths for certain values of electron temperature T_e and density N_e. In order to obtain a profile for any couple (T_e,N_e), a bilinear interpolation is performed from theoretical data. The theoretical line profile is convoluted with the instrumental broadening of the apparatus accounting also for the doppler broadening using a gas temperature T_g. The program interpolates points from the theoretical line profile to match the grid of the experimental data set. Any background in the experimental data is zeroed so that the data is directly comparable to the theoretical profiles.

Model	Constraint on N_e (cm^{-3})	Constraint on T_e (K)
VCS	$10^{10} \leq N_e \leq 10^{18}$	$2500 \leq T_e \leq 1.610^5$
MMM	$10^{10} \leq N_e \leq 10^{19}$	$2500 \leq T_e \leq 1.310^6$
CS	$10^{14} \leq N_e \leq 10^{19}$	$1042 \leq T_e \leq 1.710^6$

Table 1: Plasma parameters validity range.

2.2. Plasma diagnostics using molecular spectra

Plasma characterization using molecular spectra is done on the basis of common fitting approaches consisting of the minimization of the functional defined by the Root Mean Square Error (RMSE) between the experimental spectrum and the spectrum calculated under various equilibrium assumptions. The theoretical spectra required to determine the RMSE are calculated on the basis of an advanced tool developed and available at the EM2C laboratory and so-called High Temperature Gas Radiation (HTGR) code [12]. Assuming thermal equilibrium, the temperature $T_{thermal}$ is obtained applying the fitting procedure on experimental spectra normalized to unity, which consist in the minimization of the functional expressed as:

$$RMSE\,(T_{thermal}) = \sqrt{\frac{1}{N}\sum_{i=1}^{N}\left(\bar{S}_{\lambda_i}^{exp} - \bar{S}_{\lambda i}^{theo}(T)\right)^2} \quad (6)$$

where $\bar{S}_{\lambda_i}^{exp}$ (resp. $\bar{S}_{\lambda_i}^{theo}$) designates the normalized experimental spectrum (resp. calculated spectrum) and N is the number of experimental points in the considered spectral range.

2.2.1. Vibrational non equilibrium assessment

The HTGR code can support various assumption concerning the distribution of emitting levels. Additionally to the thermal situation, an other assumption is considered to determine the population of the vibrational excited states from the vibrational band of a molecular system. In the frame of thermal equilibrium model, the population of an energy level (n,v,j) is expressed as:

$$n_{n,v,j} = N_{tot} g_s \frac{(2J+1)}{Q_{int}(T_{LTE})} \times exp\left(-\frac{E_{el}(n) + E_{vib}(n,v) + E_{rot}(n,v,J)}{kT_{LTE}}\right) \quad (7)$$

where $Q_{int}(T_{LTE})$ is the internal partition function, N_{tot} is the total population of the considered species and g_s is the nuclear spin statistical factor. Assuming rotational equilibrium, the population can be expressed as a function of the population of the vibrational levels n_v:

$$n_{n,v,j} = n_v g_s \frac{(2J+1)}{Q_{rot,v}(T_{rot})} \times exp\left(-\frac{E_{rot}(n,v,J)}{kT_{rot}}\right) \quad (8)$$

where $Q_{rot,v}(T_{rot})$ is the rotational partition function. The determination of the variables (T_{rot},$n_{v_{k=1,vmax}}$) consists in the minimization of the functional defined as:

$$RMSE\,(T_{rot}, n_{v_k}) = \sqrt{\frac{1}{N}\sum_{i=1}^{N}\left(\bar{S}_{\lambda_i}^{exp} - \bar{S}_{\lambda_i}^{theo}(T_{rot}, n_{v_{k=1,vmax}})\right)^2} \tag{9}$$

3. Supersonic air plasma jet in VKI Plasmatron facility

The VKI Plasmatron Inductively Coupled Plasma (ICP) source uses a high frequency, high power and high voltage generator (400 kHz, 1.2 MW, 11 kV), feeding a single-turn inductor [13]. For the present experiments, the Plasmatron is operating at 350 kW power and 1.8 g/s mass flow rate. Supersonic plasma jet is obtained by expanding the plasma through a convergent nozzle into a chamber maintained at low pressure. Multiple reflections of expansion waves originating from the throat of the nozzle gives rise to complex structures of compression and expansion zones in the jet. The presence of non monotonic pressure

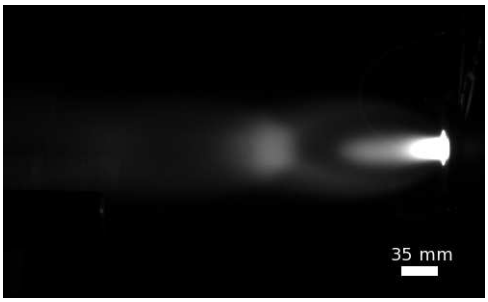

Figure 1: Supersonic air plasma jet (2 mbar chamber pressure).

and velocity gradients causes the plasma to propagate through various stage of equilibrium states along the axis of the jet. In the present study, the pressure in the chamber is maintained at 2 or 10 mbar corresponding respectively to a highly underexpanded figure 2 and underexpanded figure 1 situation while the pressure in the reservoir is maintained at 50 mbar. A basic analysis of the oscillation of the emission in the supersonic jet enables to evidence peaks at 600 and 1200 Hz induced by the three phase rectifier operating at 300 Hz. Lower frequency peaks were also observed at 170 and 340 Hz.

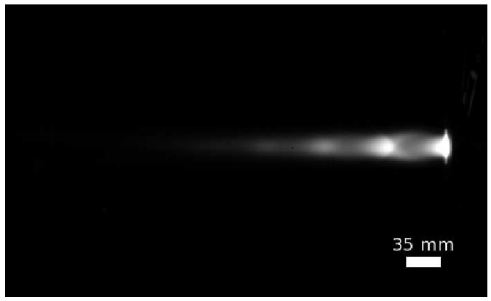

Figure 2: Supersonic air plasma jet (10 mbar chamber pressure).

3.1. Supersonic regime

The supersonic plasma flows encountered in this study evidence a pressure at the exit of the convergent being higher than in the chamber. In order to equilibrate the pressure difference at the exit of the convergent, expansion waves are created and directed towards the jet axis which are then reflected in the direction of the plasma jet boundaries. These expansion waves direct the flow towards the edge of the plasma jet, creating a radial expansion in addition to the axial expansion. The edges of the expansion zone are bright because of the reflection of the expanding flow by the cold dense surrounding gas, which gives rise to the so called barrel shocks. Reducing the chamber pressure, leads to the creation of a Mach disk downstream of the first expansion cell, leading to subsonic velocities downstream of this region with an increase of the local temperature and pressure.

3.2. Nonequilibrium diagnostics using OES

Optical Emission Spectroscopy (OES) allows to obtain information on excited states densities without disturbing the flow. Accurate measurements rely on stationary flow emission and low contamination of the jet. A conventional OES technique was set up and applied in a large spectral range on a supersonic underexpanded air plasma jet in the first expansion zone at 25 mm from the exit of the convergent throat. We focus our study on the spectral domain that includes the N_2^+ First negative system Δv=+1 and the H_β hydrogen line. The discharge is generated inside the torch and the plasma jet flows into the test chamber maintained at a constant pressure of 10 mbar through a 35 mm diameter nozzle exit. The line of sight plasma jet emission is collected through an aperture and then focused with a fused silica lens onto the entry of a Acton Series monochromator of 75 cm focal lengths. The spectrometer is combined with a ICCD PI-MAX

camera with a frame of 1024×1024 pixels of 12.8 μm side. Emission issued from the jet is spatially resolved in the radial direction. A radial slice of about 19 cm height was optically conjugated using a 100 mm focal lens onto an image with a magnification factor of 0.07. It allows to capture the whole radial profile of the jet onto the CCD screen of the camera with a spatial resolution of about 180 microns. The radiation from the N_2^+ First negative system was recorded using a 150 groves/mm grating as the hydrogen line H_β spectral resolution was improved by using a 1200 groves/mm grating in order to resolve Stark broadening contribution. The corresponding spectral resolutions were measured to be respectively 0.5 nm and 0.06 nm, setting the entrance slit of the monochromator to 3 microns. The recorded spectra were calibrated in absolute intensity combining a ribbon tungsten lamp and its documented absolute radiance and a deuterium source. At the conditions reported here, the air mixture is assumed to be optically thin and proper Abel inversion was applied on measured spectra allowing to rebuild the spectral emission ($W.m^{-3}.sr^{-1}.\lambda^{-1}$). Calibrated spectra at the plasma jet center line are shown in figure 3. The displayed radiative signature is dominated by oxygen and nitrogen atomic lines in the visible spectral range. The N_2^+ First Negative system is hardly detected.

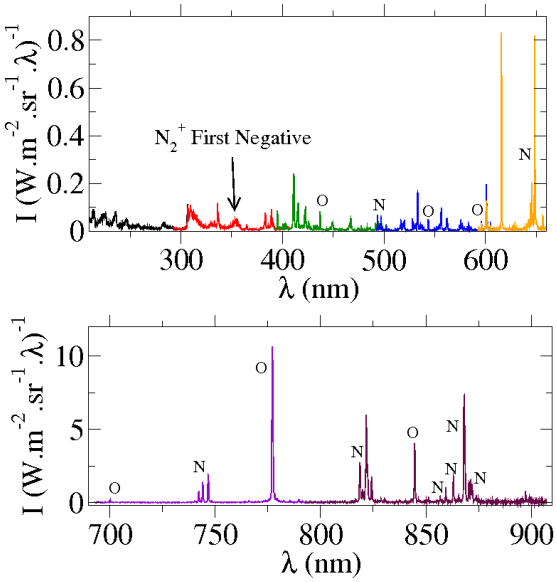

Figure 3: Typical radiative signature of supersonic air plasma jet in the first expansion zone (r = 0 mm, z = 25 mm).

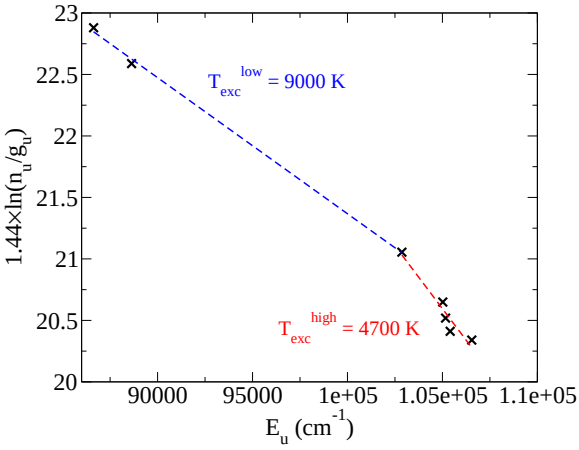

Figure 4: Boltzmann diagram at the center of the jet using oxygen atomic lines (r = 0 mm, z = 25 mm).

3.2.1. *Departure from equilibrium of the electronic excited states*

Boltzmann diagram as plotted in figure 4 using atomic oxygen lines at the center of the jet. The useful spectroscopic data are recalled in Appendix A. The diagram does not comply with a single straight line, indicating that departure from Boltzmann equilibrium occurs. Two straight lines are fitted on the experimental points to derive the excitation temperature of lower states T_{exc}^{low} at a temperature of about 9000 K and higher states T_{exc}^{high} at a temperature of about 4700 K. Provided pLSE starts at the higher excited states $T_e = T_{exc}^{high}$, the plasma is characterized by an underpopulation of lower excited states which is representative of a recombining plasma.

3.2.2. *Assessment of vibrational equilibrium*

Detailed energy distribution among the quantum states within the vibrational mode is essential to characterize non thermal plasmas issued from supersonic nozzle expansion. The fitting procedure is executed on Abel transformed spectra at 1.7 cm from the jet center line where molecular radiative contribution is not overlapped by atomic lines. Figure 5 exhibits the distribution of the vibrational bands of N_2^+ First Negative system $\Delta v=+1$ calculated at 9000 K with an apparatus function of 0.06 nm. Taking this spectral resolution, we can clearly distinguish bands from v=0 to v=4. For vibrational level higher than 5, we can notice vibrational band inversion which allows to execute the minimization procedure on a large amount of vibrational levels despite the small spectral win-

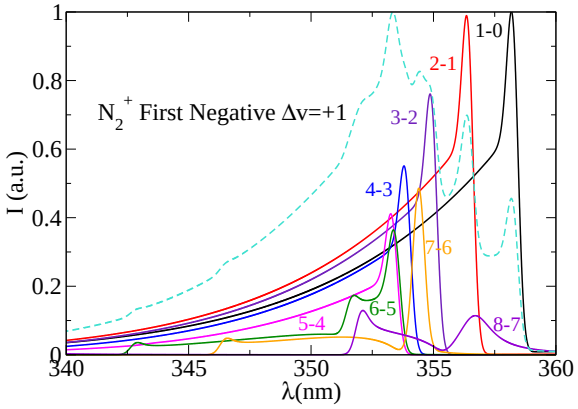

Figure 5: Vibrational bands distribution of N_2^+ First Negative system $\Delta v=+1$.

dow. Assuming thermal equilibrium, best fit is obtained 1.7 cm from the jet center line with a temperature $T_{thermal}$= 8357 K. The calculated spectrum is in fairly good agreement with the experimental spectrum figure 6 (a), suggesting for proximity to rotational and vibrational equilibrium. Accounting for rotational equilibrium only, the vibrational distribution is determined. Best fit is presented in figure 6 (b). This method allows to improve the matching between experimental and calculated spectra. In this case, the RMSE is 2% lower than in the thermal equilibrium case. The rotational temperature is found to be T_{rot}=7026 K. Vibrational population is plotted on figure 7. Neglecting the weak contribution of the vibrational level v=8, a straight line can be fitted on the logarithm of the vibrational population and by using the energy of each level we obtain a vibrational temperature T_v= 8800 K.

3.2.3. Electronic density measurement

Fitting of experimental data is performed with MMM data at the center of the jet. Contamination in the wings of the hydrogen H_β line is excluded by the minimization procedure. The best fit obtained is presented in figure 8 corresponding to an electronic density of 3.0 10^{-20} m^{-3}. The MMM data tables have been calculated for an emitter-perturber reduced mass of 0.5 which corresponds to a pure hydrogen plasma and we take the electronic temperature T_e equal to the excitation temperature of high electronic excited states T_{exc}^{high} providing that pLSE is effective. CS data would permit to account for other perturbing species and also to account for non equilibrium between electrons and heavy particles. This study will be part

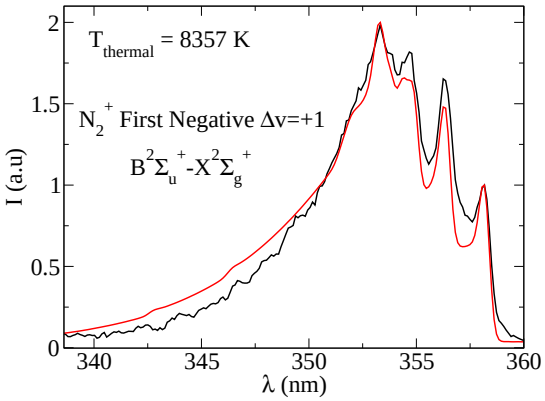

(a) Thermal equilibrium assumption.

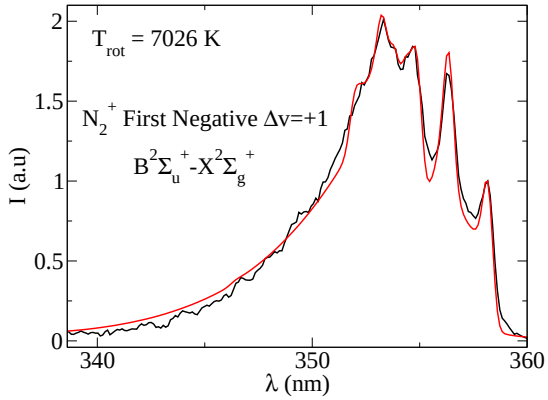

(b) Rotational equilibrium and vibrational nonequilibrium assumption.

Figure 6: Best fit between experimental spectrum (black) and calculated spectrum (red) (r = 17 mm, z = 25 mm).

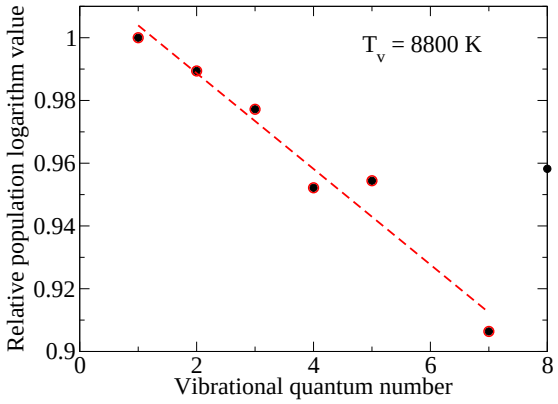

Figure 7: Relative population of vibrational energy levels for N_2^+ First Negative system $\Delta v=+1$ vibrational band (r = 17 mm, z = 25 mm).

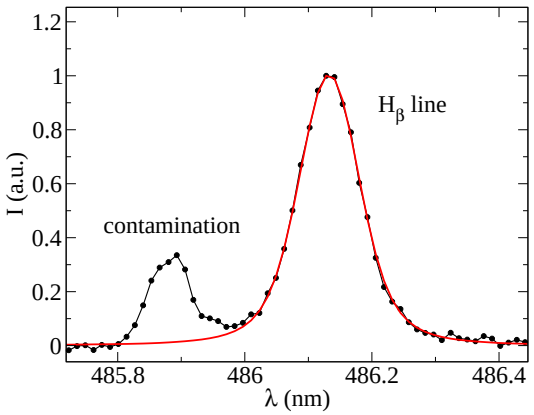

Figure 8: Best fit between experimental (black) and theoretical (red) hydrogen H_β line profile (r = 0 mm, z = 25 mm).

of further investigation. It should be noted that air plasma was not seeded with water or hydrogen. The intensity of the hydrogen lines was fluctuating which does not prevent from performing a diagnostic based on line broadening. The contamination in figure 8 might be caused by a Fe atomic line.

4. Investigation of microwave sustained plasma source

The MPT plasma source was built in VKI on the basis of a magnetron head (MH3.OW-S1 Richardson Electronics) operating at 2.45 GHz with a SM1150T power supply to produce microwave power in the kilowatt range transmitted through a rectangular waveguide (WR 340 adapted for λ =12.24 cm wavelength) to the gas flowing in a quartz tube of 30 mm inner diameter similarly to [14].

4.1. Plasma jet unsteadiness

The fluctuating part of the intensity has been investigated by means of high speed imaging measurements using a Phantom v7.0 8 bits CCD camera at an acquisition rate of 1 kHz. The examination of the unsteady feature of the flow emission provides useful information about the effect of microwave power oscillation on thermal inhomogeneity taking place in the plasma flow. Simple processing has been applied to high speed frame records to show the presence of regions inside the jet that are hotter or colder than the steady contribution. The FFT of optical emission fluctuation was executed to show the heating modulation at well defined frequencies. Figure 9(a,b) shows

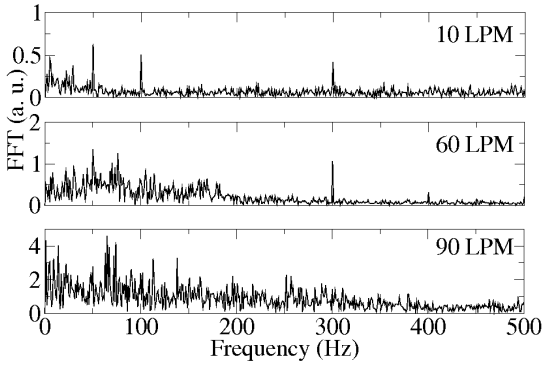

(a) 2kW air plasma jet.

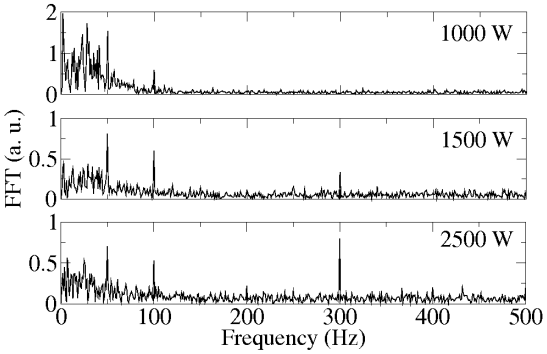

(b) 15 LPM air plasma jet.

Figure 9: FFT of an air plasma jet emission fluctuation on the axis at 1 cm from the waveguide.

the FFT operated on a spatial pixel located at 1 cm from the waveguide at the plasma center line for an air mixture at different power and flow rates. At 10 LPM, the spectrum is mainly composed of well defined frequencies above 50 Hz (50, 100 and 300 Hz) related to the coherent dynamic of the jet. Increasing the flow rate leads to the damping of these peaks vanishing into noisy background rising towards the low frequency range. These coherent peaks result from the modulated Joule heating of the feeding circuit. It has been observed that operating with a forwarded power slightly above the minimum threshold value required to sustain the plasma leads to a highly unstable plasma flow. The instability of the flow resulting from thermal inhomogeneities generated by the power modulation is damped by increasing the power. Figure 9(b) shows the effect of the input power on the plasma jet dynamics. As the power is increased, the spectral dynamics of the oscillations is mostly driven by peaks above 100 Hz as moderate frequencies contribution tends to fade.

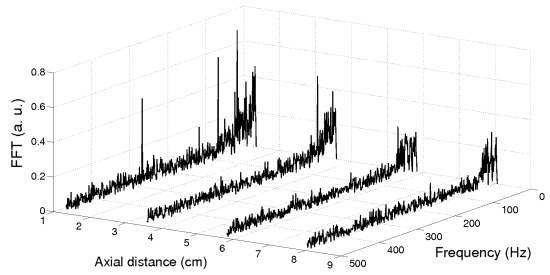

Figure 10: FFT of an air plasma jet emission fluctuation as a function of the distance from the waveguide.

4.2. Forwarded and reflected power monitoring

Forwarded and reflected microwave power were monitored at different flow rates and power in an air plasma. An Alter RD8400 power sensor is used to measure the microwave signal at 2.45 GHz previously attenuated at 60 dB by the circulator device. It allows to measure the maximum waveguide power with a full scale 0-10 Vdc output voltage. Alternative measurements have been performed on the forwarded and reflected signals. Temporal and frequential forwarded and reflected power signals are plotted in Figure 11(a,b). The effect of the flow rate variation on the reflected power is considerable. As the flow rate increases, the amplitude of the oscillations evolves from a coherent situation to random variation associated to noisy dynamic increasing towards low frequencies below 100 Hz. It is in agreement with plasma optical emission light dynamic oscillation. Coupling microwave power to the plasma requires the impedance between the discharge and the microwave power source to be matched. A common means to achieve this match is to insert a metallic element into the waveguide, which was performed here using screws. Since an impedance mismatch has phase and amplitude components, both position and depth of insertion of the matching element must be adjusted. Three screws, manually adjusted, are positioned inside the waveguide and the effect of the depth of the insertion was studied. For different configurations, the efficiency of the plasma source is illustrated on Figure 12, where the reflected RF power is plotted versus the forward RF power. We observe that the optimal configuration of the screws allows more than 90 % efficiency ($1 - \left(P_{reflected}/P_{forwarded}\right)$). Bad impedance matching can decrease the efficiency to about 75 % efficiency.

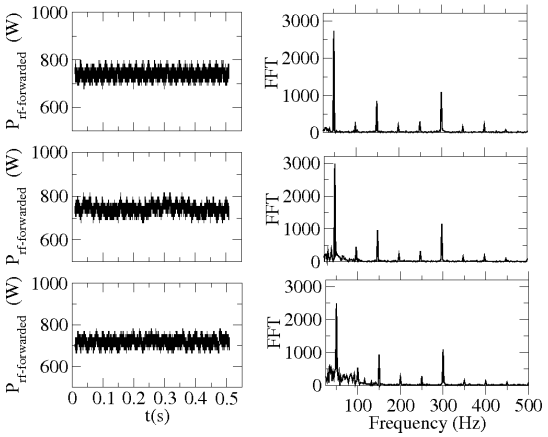

(a) Forwared power (top to bottom: 5, 10, 20 LPM).

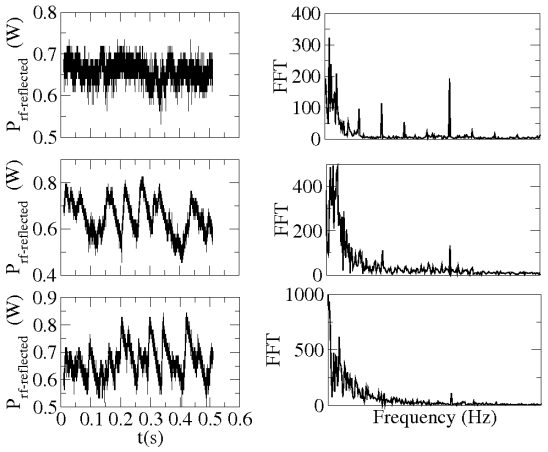

(b) Reflected power (top to bottom: 5, 10, 20 LPM).

Figure 11: Microwave power and associated FFT signal for air plasma at different flow rate.

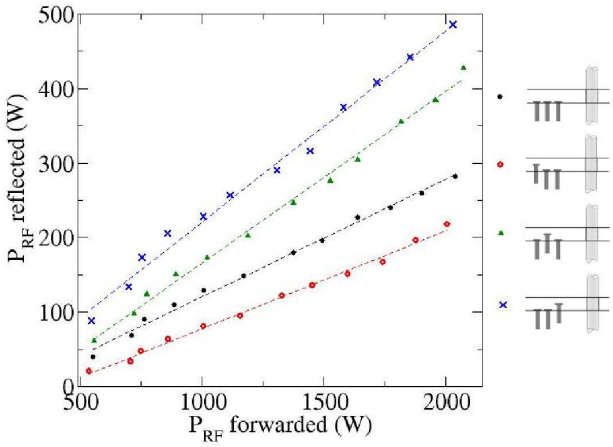

Figure 12: Reflected power versus forwarded power for different configurations of the impedance matching screws

4.3. Low resolution spectra examination

The examination of the radiative transitions of air, N_2 and CO_2 plasmas was performed by means of a low resolution OES bench at the jet center line. Acquired raw data are displayed in Figure 13(a) for various operating powers. The displayed spectra are characterized by significantly different contribution depending on the operating gas. Air radiative signature is mainly constituted of molecular emission of O_2 Schumann-Runge in the spectral domain below ~ 600 nm and of NO systems ($\beta, \gamma, \delta, \epsilon$) peaking at 250 nm. N_2^+ First Negative and N_2 Second Positive systems are the main contributors in pure N_2 plasma between 290 nm and 450 nm. CO_2 plasma emission is constituted of both molecular transitions from C_2 Swan system and atomic lines of Oxygen and Carbon. Air plasma emission spectrum is less appropriate for temperature determination by means of a spectra fitting approach in comparisons with N_2 and CO_2 radiative signatures. Indeed, air plasma emission in the visible range exhibit a poor dynamic detrimental for accurate fitting and the NO systems lying in the UV are self absorbed preventing a direct access to the local emission. In Figure 13(b), normalized radiative signatures of N_2 plasma are presented at different input powers. The poor dynamic change in the shape of the spectra indicates for a weak change in temperature. An additional microwave power contributes to the expansion of the plasma in the radial direction associated with an increase of the light emission intensity rather than a change in temperature. It is consistent with the observations in [15].

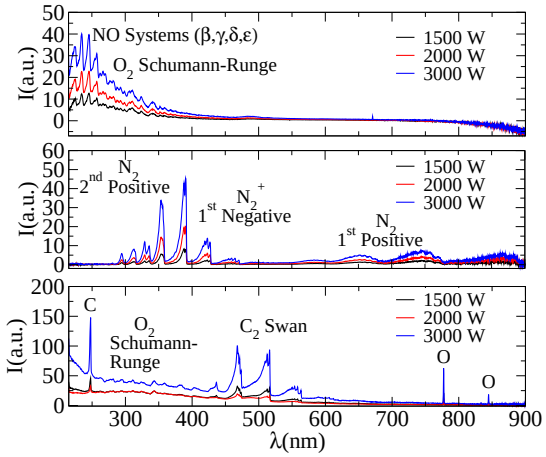

(a) Typical radiative signature of air, N_2 and CO_2 plasmas using different input power.

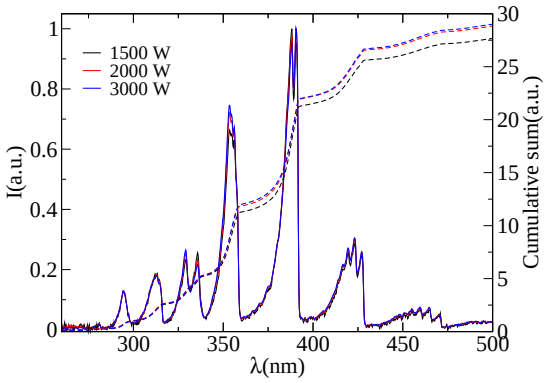

(b) Normalized N_2^+ First Negative system of pure N_2 plasma using different input power.

Figure 13: Low resolution spectra.

5. Conclusion

Various diagnostics have been used to characterize a supersonic air plasma jet in the first expansion zone. Plasma parameters have been derived at the center of the jet where diagnostic involve atomic contribution of oxygen species. Parameters derived from molecular radiation were studied at 1.7 cm from the jet center line where the contribution of N_2^+ First Negative system $\Delta v=+1$ is clearly defined. The lack of information about the static pressure and the non equilibrium distribution of oxygen atomic excited states make the determination of excitation temperature questionable leading to a temperature of the higher excited states of about T_{exc}^{high}= 3800 K. Assuming pLSE T_{exc}^{high} has been used to determine the electron number density by fitting experimental hydrogen H_β line onto theoretical lineshape. Despite weak contamination on the wing of the experimental hydrogen line, a good fit is obtained for an electron density corresponding to 3.0 10^{-20} m^{-3}. The presence of molecular radiation on the edge of the plasma jet allows us to probe rotational and vibrational levels and indicates a proximity to rotational and vibrational equilibrium. The rotational temperature has been determined by either assuming thermal equilibrium or assuming rotational equilibrium and vibrational non equilibrium. In the first case, T_{rot}=$T_{thermal}$= 8357 K, with a fairly good agreement between experimental and calculated spectra. In the second case, the fitting is improved and leads to a rotational temperature T_{rot}=7026 K. Vibrational temperature obtained by fitting the experimental vibrational levels with a straight line gives a temperature T_v= 8800 K. Description of microwave sustained plasma jet structures has been established within a large range of operating conditions (0-≈100 LPM, 1-≈3.5 kW) for

an air mixture at atmospheric pressure. Flow rate and input power contribute highly to the jet dynamics and shape. The fluctuating emission of the plasma jet has been monitored by means of high speed camera imaging. Plasma jet unsteadiness was clearly consistent with the powering circuit oscillations. The high efficiency of this source was measured at about 0.9 in best configuration for an air plasma jet. Although the dielectric properties of the plasma vary with changes in temperature and chemical composition, a single matching screws configuration corresponding to the highest efficiency will be retained and used for further experiments. Low resolution spectra were measured using air, N_2 and CO_2 gases. It indicates that increasing the microwave power contributes to the expansion of the plasma in the radial direction of the jet. Experimental campaigns, not presented here, have ensured that MPT might be considered as a valuable source to provide an appropriate reservoir of high temperature gas close to equilibrium.

Appendix A. Spectroscopic data

O lines			$D_e = 109837.02cm^{-1}$		
501.8782	4.2810^5	86 625.757	106 545.354	3	5
501.9291	7.1310^5	86 627.778	106 545.354	5	5
543.5178	$7.74\ 10^5$	86625.757	105019.307	3	5
543.5775	$1.29\ 10^6$	86627.778	105019.307	5	5
543.6862	$1.80\ 10^6$	86631.454	105019.307	7	5
595.8386	$6.80\ 10^5$	88630.587	105409.008	3	5
595.8386	$3.78\ 10^5$	88630.587	105409.008	3	3
595.8584	$2.27\ 10^5$	88631.146	105409.008	5	5
595.8584	$2.52\ 10^4$	88631.146	105409.008	5	3
595.8584	$9.06\ 10^5$	88631.146	105409.008	5	7
604.6233	$1.05\ 10^6$	88630.587	105165.232	3	3
604.6438	$1.75\ 10^6$	88631.146	105165.232	5	3
604.6495	$3.50\ 10^6$	88631.303	105165.232	1	3
615.5971	$5.72\ 10^6$	86625.757	102865.655	3	3
615.6778	$5.08\ 10^6$	86627.778	102865.547	5	7
615.8187	$7.62\ 10^6$	86631.454	102865.506	7	9
777.1944	$3.69\ 10^7$	73768.200	86631.454	5	7
777.4166	$3.69\ 10^7$	73768.200	86627.778	5	5
777.5388	$3.69\ 10^7$	73768.200	86625.757	5	3
844.6247	$3.22\ 10^7$	76794.978	88631.303	3	1
844.6359	$3.22\ 10^7$	76794.978	88631.146	3	5
844.6758	$3.22\ 10^7$	76794.978	88630.587	3	3

Table A.2: Spectroscopic data of the considered O emission lines used for air plasma [16].

Acknowledgments

The author would like to acknowledge the financial support of the European Commission within the frame of the 7^{th} Frame Program Project FP7-SPACE209-242311: Planetary Entry Integrated Models.

References

[1] V.Sember, D.V.Gravelle, M.I.Boulos, Spectroscopic study of a supersonic plasma jet generated by an ICP torch with a convergent-divergent nozzle, Journal of Physics D: Applied Physics Vol.35 (2002) pp.1350–1361.

[2] S.E.Selezneva, M.Rajabian, D.Gravelle, M.I.Boulos, Study of the structure and deviation from equilibrium in direct current supersonic plasma jets, J. Phys. D: Appl. Phys. Vol.34 (2001) pp.2862–2874.

[3] M.C.M.van de Sanden, J.M.de Regt, D.C.Schram, Recombination of argon in an expanding plasma jet, Physical review E Vol.47-Number 4.

[4] L.Robin, P.Vervisch, B.G.Cheron, Experimental study of a supersonic low-pressure nitrogen plasma jet, Phys. Plasma Vol.1 - NO.2 (1994) pp.444–458.

[5] R.Yano, V.Contini, E.Plönjes, P.Palm, S.Merriman, S.Aithal, I.Adamovich, W.Lempert, V.Subramaniam, J.W.Rich, Supersonic nonequilibrium plasma wind-tunnel measurements of shock modification and flow vizualization, AIAA Journal Vol.38 (2000) No.10.

[6] M.Inutake, K.Yoshino, H.Tobari, H.Fukui, R.Sato, K.Hattori, A.Ando, Production of a Supersonic Plasma Flow through a Laval Magnetic Nozzle, Proc. of 26th Int. Conf. on Phenomena in Ionized Gases,1, (2003) pp.127–128.

[7] X. Tu, J. Yan, L. Yu, K. Cen and B. Cheron, The nature of the fluctuations in a double argon-nitrogen plasma jet, Applied Physics Letter Vol.91.

[8] Characterization of a DC plasma torch through its light and voltage fluctuations, N. Singh, M. Razafinimanana, J. Hlina, Journal of Physics D: Applied Physics Vol.33 (2000) pp.270–274.

[9] C. R. Vidal, J. Cooper, E. W. Smith, Hydrogen Stark-Broadening Tables, The Astrophysical Journal supplement Vol. 214.

[10] B. W. Acon, C. Stehle, H. Zhang, A. Montaser, Stark-broadened hydrogen line profiles predicted by the model microfield method for calculating electron number densities, Spectrochimica Acta Part B Vol. 56 (2001) pp. 527–539.

[11] M. A. Gigosos, M. A. Gonzalez, V. Cardenoso, Computer simulated Balmer-alpha, -beta and -gamma Stark line profiles for non-equilibrium plasmas diagnostics, Spectrochimica Acta Part B Vol. 58 (2003) pp. 14891504.

[12] M. Y. Perrin, P. Rivière, A. Soufiani, Radiation database for Earth and Mars entry, Von Karman Lecture Series RTO-EN-AVT-162.

[13] B. Bottin, M. Carbonaro , S. Zemsch and G. Degrez, Aerothermodynamic design of an inductively coupled plasma wind tunnel, 32^{nd} AIAA Thermophysics Conference, Atlanta, USA AIAA paper 97-2498.

[14] Y. Babou, Transferts radiatifs dans les plasmas de mélange CO_2-N_2: base de données spectroscopiques, étude expérimentale et application aux rentrées atmosphèriques, Laboratoire d'Enèrgétique Moléculaire et Macroscopique, Combustion (EM2C) du CNRS et de l'ECP, Paris.

[15] A. V. Timofeev, Theory of microwave discharges at atmospheric pressures, Plasma Physics Reports Vol. 23, no. 72, pp. 158 164.

[16] NIST atomic spectra database , http://physics.nist.gov/PhysRefData/ASD/index.html.

Methodology for Ablation Investigations of Innovative Ablators in the VKI Plasmatron Facility Including First Results on a Carbon Fiber Preform

Bernd Helber

Aeronautics and Aerospace Department, von Karman Institute for Fluid Dynamics, Belgium, helber@vki.ac.be

Supervisor: Thierry Magin

Assistant Professor, Aeronautics and Aerospace Department, von Karman Institute for Fluid Dynamics, Belgium, magin@vki.ac.be

University Supervisor: Annick Hubin

Professor, Department of Electrochemical and Surface Engineering, Vrije Universiteit Brussel, Belgium, anhubin@vub.ac.be

Abstract

The continued interest in planetary entry probes, sample return missions, and the eventual extension to a manned mission to Mars demand ground testing of ablative materials as well as sophisticated modeling of their response to reentry environment. They are the only solution for such high speed reentries as no material is known to withstand the high thermal loads. Following the current developments of a new class of low-density, carbon/resin composite ablators, new efforts were initiated at the VKI on ablation research. This paper first summarizes the progress made on ablation testing in the VKI Plasmatron facility over the last years and presents a strategy for future investigations of innovative low-density ablators. Finally, preliminary results obtained on a carbon fiber preform are discussed, which is the basic material for new class ablators. Scanning-Electron-Microscopy was used to examine fiber ablation at microscale level and micrographs are shown revealing strong oxidation mechanisms.

Keywords: ablation, high enthalpy plasma flows, gas-surface interaction, emsission spectroscopy, scanning electron microscopy

1. Introduction

Motivation

On July 21, 2011, *Atlantis* landed safely back on earth after fulfilling the very last space shuttle mission, commencing the end of the first and so far only manned spacecraft with a reusable heat shield. The Russian *Soyuz* capsule, designed in the 1960s, is now exclusively serving the International Space Station (ISS) and is together with Chinese's *Shenzhou* (1992) the only transporter currently used for human spaceflight. ESA is developing an Advanced Reentry Vehicle (ARV) for crew and cargo transportation from the ISS, whereas NASA is planning a Multi-Purpose Crew Vehicle (MPCV) for deep space exploration with the final aim of a crewed Mars landing.

Following the launch of the Mars Science Laboratory (MSL) on November 26, 2011, with one of its scientific goals being a plan for human missions to Mars, the next steps will be to identify, develop and qualify required technologies for safely returning Martian samples. For such spacecraft entering a planet's atmosphere, high requirements are put on the thermal protection system (TPS) in order to shield crew and payload from the severe heating.

Problem statement

Since the strong efforts spent in the 1960's on the Apollo program [1; 2], ablative heat shields are the first choice for space capsules due to their efficiency and reliability (Fig. 1). Especially for very high reentry speeds exceeding 10km/s, typical for the new missions of ESA and NASA, ablators are the only solution as no known material is able to withstand the high thermal loads without degrading. Ablative heat shields take advantage of this property as they are able to dissipate the high heat fluxes through chemical and

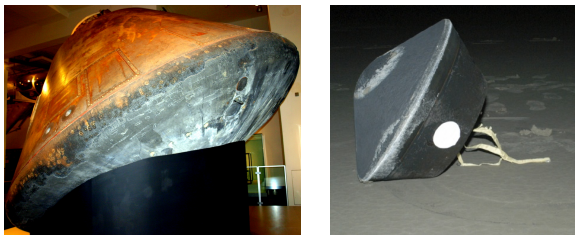

Figure 1: left: Apollo 10 with ablative heat shield after reentry (fastest manned reentry, 11.08 km/s, 1969), right: NASA Stardust probe after reentry (fastest man-made reentry object, 12.9 km/s, 2006)

physical decomposition, transforming the thermal energy into mass loss and recession, whilst the remaining solid material insulates the vehicle substructure. This makes selection of the TPS material and thickness design the two key performance parameters and inaccuracies in the prediction tools for TPS design can be fatal for the crew or the success of robotic missions.

The estimation of TPS sizing is a complex task and the prediction tools are still inherited from the Apollo program [3; 4]. Besides, a new generation of low density carbon/resin composite ablators is currently being developed. They are made of a carbon fiber preform impregnated in phenolic resin, such as PICA [5; 6] and ASTERM [7], developed by NASA and ESA, respectively, for high-speed entry missions. New high fidelity material response models are proposed [8] in order to take into account the micro-structure of the porous material. This calls for a sound methodology in numerical and experimental research to understand the complex gas-surface interaction and material response in plasma flows.

After first recalling the ablation process, this paper will review the efforts undertaken at the von Karman Institute on ablation testing during the last years and come up with a complementary approach for characterization of the performance of innovative ablators. This new methodology, existing of atmospheric plasma test in high enthalpy flows and microscale analysis, has been applied to a carbon fiber preform, which serves as basic material for new generation ablators. Preliminary results of carbon fiber preform ablation tests will be presented at the end of the paper.

2. Ablation of charring materials

2.1. The ablation process

The processes through which ablators are able to accommodate high heat fluxes are balanced between surface radiation, phase transitions (melting, sublimation) as well as chemical reactions (charring, oxidation) on the surface and inside the material. To achieve high performance characteristics of ablative materials mostly composite materials are used for the ablative heat shield. When subjected to increasing temperature, the virgin material successively transforms following two mechanisms (Fig. 2):

1. During ***pyrolysis*** the phenolic resin is progressively carbonized into a low density, porous char and loses around 50% of its mass producing pyrolysis gases by vaporization. The pyrolysis gases are transported out of the material by diffusion and convection and exhaust into the boundary layer, providing a further barrier for the heat exchange (blowing) and undergo additional chemical reactions, consuming more heat. Making usage of polymers such as phenolic resins for the matrix of the composite takes advantage of their endothermic degradation nature, thereby absorbing energy, and serving as a binder for the other components [9].

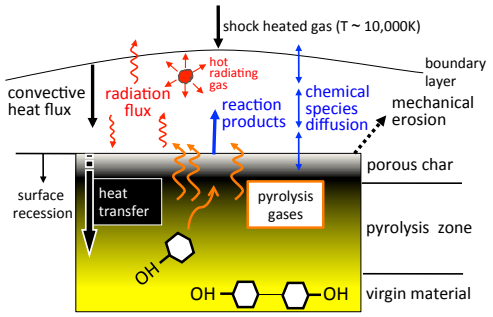

Figure 2: Ablation and pyrolysis processes of a charring material

2. ***Ablation*** of the char layer (composed of the carbonized resin and the remaining carbon fibers) is then promoted by heterogeneous chemical reactions, phase change and mechanical erosion (e.g. spallation), altogether leading to recession of the material. The rate at which an ablator recesses is therefore a functional consequence of its intended prevention of heat conduction and strongly coupled to the aerothermal conditions it encounters. In other words, the material will primarily respond with a higher ablation rate to increased heating whilst the heat conducted to the bondline will stay constant. This illustrates the great importance of material response models to accurately predict recession of the material. However, due to lacking good experimental data, this quantity remains as one of the largest uncertainties in material response analysis [10].

2.2. Existing modeling tools

During the Apollo program, strong efforts were invested to develop models for the prediction of complex gas surface interaction for thermal protection materials (TPMs). Those models, developed for dense ablative materials, are inspired from Kendall *et al.* published in 1968 [3; 11]. They rest on major assumptions and describe ablation as a surface phenomenon occurring on a homogeneous, dense material assuming equilibrium or finite-rate chemistry in a control volume close to the wall. The very complex thermochemical problem necessitates the generation of non-dimensional ablation tables, usually referred to as *B'*-tables, for pyrolysis-gas mass flux and char consumption rate (B'_g and B'_c). The coupling strategy with the flow environment is based on considering a thin control volume where the gas-surface interactions occur and where mass balance and equilibrium chemistry are satisfied. By this, the interaction of material and flow codes are approximated through the use of heat and mass transfer coefficients.

Weaknesses of this strategy are for example the model of mass transport due to diffusion into the control volume as well as negligence of blowing the pyrolysis products into the boundary layer, what will change the boundary layer condition. The efforts now focus on developing new flow solvers that can bypass the use of *B'*-tables and to couple them to in-depth, high fidelity material response solvers. For this task, innovative experiments are necessary on multicsale level for characterization of the material degradation in high enthalpy flows and subsequent model validation.

3. First efforts on ablation testing at the VKI

Graphite is widely used as exploratory material for basic research to narrow down the physics and thermochemistry to a non-charring, purely carbonic material. This enables to focus on the ablation phenomenon in the absence of pyrolysis. Ablation studies on graphite at the VKI were initiated by Fletcher and Vancrayenest in 2005, who started with investigations of the thermochemistry of ablating graphite by means of emission spectroscopy in the 15 kW inductively coupled plasma windtunnel Minitorch [12]. Due to the limited capabilities of the Minitorch windtunnel and the necessity of high enthalpy plasmas for ablation studies, the experiments were moved to the 1.2MW Plasmatron facility [13; 14]. The work of Vancrayenest and Fletcher showed the successful integration of emission spectroscopy, providing emission spectra as well as recession and mass loss rates of a 50 mm diameter, flat faced ablating graphite piece in air and nitrogen plasmas at heat flux levels between 500 $\mathrm{kW/m^2}$ and 1500 $\mathrm{kW/m^2}$

The knowledge gained throughout those ablation tests was translated into the development of a testing methodology for charring, low-density ablators. A cork compound provided by AMORIM (P50) was tested at varying heat flux and pressure levels [15] as well as the newly developed monolythic ablator *MonA* (Lockheed Martin Space Systems, distributed by LMUK) [16; 17]. This low-density ablator is a carbon-phenolic composite, structurally reinforced by a Flex-Core honeycomb, and was a considered TPM for the NASA Orion capsule. The heat flux levels for *MonA* ablation tests reached a maximum of 4500 $\mathrm{kW/m^2}$ and the experimental setup was extended by a high speed camera for surface recession measurements. This new technique enabled in-situ measurements of the degrading surface from which the assumption of a steady ablation rate was assessed. This is pointed out in Fig. 3 where a contour plot is presented, obtained by applying edge detection filters during post-processing of the HSC images. By conversion of pixel:millimeter, the rate of recession can be estimated in-situ, contrary to only absolute pre- and post-test measurements. Furthermore, a gas-front ahead of the ablating sample was identified, which is most likely an effect of the degassing pyrolysis products. Those help keeping away the hot plasma flow from the surface before burn-off in the boundary layer, what is visible as a bright flame.

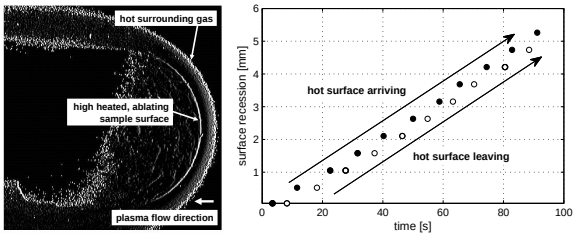

Figure 3: HSC snap-shot during ablation test showing the surface and gas-front (no shock wave); consequently the recession rate of *MonA* can be computed [16].

The radiation emitted by the reacting plasma flow can be captured by various spectroscopy tools. Time resolved emission spectroscopy was applied to ablation of *MonA* and indicative of electronically excited CN violet ($B^2\Sigma^+ \rightarrow X^2\Sigma^+$) and CN red ($A^2\Sigma_u^+ \rightarrow X^2\Sigma^+$), which was highly apparent in pure nitrogen plasma flows suggesting strong nitridation reactions.

In air plasma, the amount of CN significantly decreased pointing out dominant oxidation reactions (CO, CO_2, NO). Transient thermo-chemical mechanisms were found in nitrogen plasma, where electronically excited diatomic carbon (C_2 Swan system) was highly radiating after injection of the *MonA* sample but truncated after a few seconds. An illustrative emission spectrum recorded during sample injection into nitrogen plasma is shown in Fig. 4.

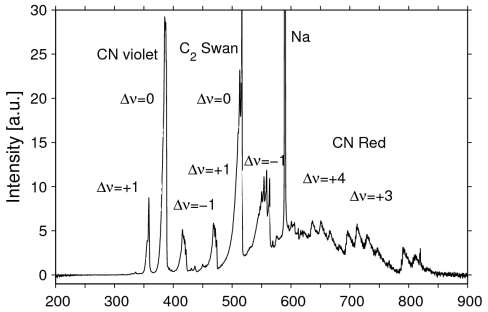

Figure 4: Emission spectrum ahead of ablating carbon resin composite sample in nitrogen test gas [16]

Utilizing combined measurements such as emission spectroscopy and high-speed-imaging illustrate the attempt of experimentally approaching the coupled physico-chemical problems, resulting from the evolution of pyrolysis products inside and outside the material, their reaction with gases coming from the freestream and the subsequent process of ablation.

It was further understood that a proper examination of tested samples has to be performed, especially at the surface and sub-surface. In this region, the char layer is subjected to ablation where for example the degradation of the carbon fibers can vary with pressure and surface temperature due to the changing diffusion mechanisms of oxygen. In particular, if oxygen is able to diffuse deep inside the material the internal structure can be weakened what leads to spallation and mechanical failure.

4. Methodology for ablator response characterization

To enable a proper design of heat shields based on porous, low-density composite ablators, a complete experimental analysis with parallel modeling is necessary. The following phenomena have to be analyzed and described accurately: **finite-rate chemistry** for pyrolysis gas, **transport phenomena in porous medium** as well as in the **boundary layer**, and **volume ablation** with an ablation zone (microscopic description of the carbon fibers).

Finally, the methodology has to be extended by an extrapolation strategy of the ground-testing conditions to real flight values, combining experimental data and numerical models. A flight extrapolation methodology was implemented at the VKI for application to reusable TPMs, which has to be approached and modified in order to be applied to the proposed work on ablative materials.

4.1. Ablation thermochemistry in high-enthalpy flows

The 1.2 MW Plasmatron facility [18] is extensively utilized at the VKI for ground-testing in atmospheric entry flows. In-situ measurements of a new generation of low density ablative materials will be performed for characterization of:

1. **Material response** to plasma exposure (temperature, heat transfer, ablation rate)
2. **Flow field** (surrounding gas phase, effect of "blowing" due to outgassing products)
3. **Radiation field** (identification and quantification of molecules and atoms such as C, C_2, CN, CO).

A schematic of the experimental setup comprising optical diagnostic bench for emission spectroscopy, high-speed-camera, and 2-color pyrometer can be found in Fig. 5. The successful application of emission spectroscopy encouraged the extend of the experimental setup by two more emission spectrometer in order to examine the ablation thermochemistry not only temporally but also spatially. The optical diagnostic bench consists of a light collection system, an optical fiber and the spectrometer. The light emitted by the plasma is collected through a variable aperture and focused by a converging lens (750 mm focal length, LA4745) via two mirrors to the entry of three 600 μm diameter optical fibers. The optics are aligned perpendicular to the flow and tangential to the test sample surface. By this, three points with variable distance (by the magnification and arrangement of the fibers) along the stagnation line through the boundary layer are imaged onto the three optical fibers. The fibers lead to three HR-4000 spectrometers which cover a broad spectrum in the desired range (200-1100 nm), suitable to rapidly determine radiating transitions of atoms and main molecular bands. The fixed entrance slit width of 5 μm and a 300 groove/mm grating lead to a typical resolution of approximately 0.6 nm (specification of supplier: 0.03-1.0 nm, depending on configuration). Calibration of the whole system in relative intensity, consisting of the light collection mechanism and spectrometer efficiencies, is

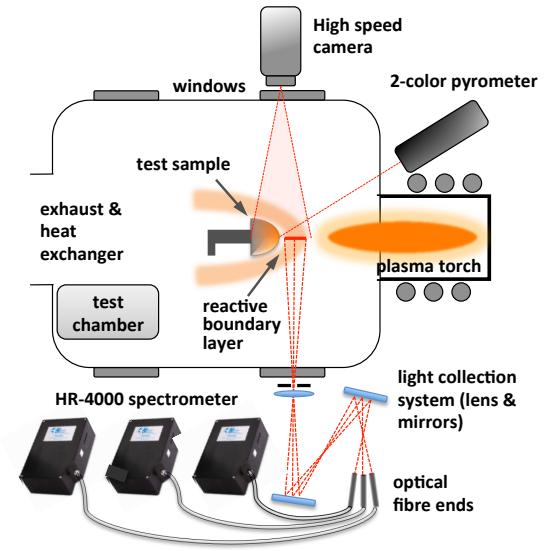

Figure 5: Emission spectroscopy setup applied to Plasmatron using three identical spectrometer focused on the reactive boundary layer ahead of the sample combined with HSC-imaging

performed using a deuterium lamp in the UV range (< 400 nm) and with a tungsten ribbon lamp (OSRAM WI 17G) in the visible range (> 400 nm), hence, obtained intensities are relatively comparable throughout the different tests.

Surface temperature measurements are carried out using a two-color Raytek Marathon MR1S-C pyrometer (0.75 − 1.1 µm, T_{max} = 3000°C). By using two separate narrow wavelength bands and under the assumption of an emissivity being independent of the wavelength, the surface temperature of a gray body can be measured independently of its emissivity. Calibration of the two-color pyrometer performed with a blackbody radiation source gave an uncertainty of $\delta T_S = \pm 10$ K.

4.2. *Multiscale analysis of porous & fibrous materials*

Tested and virgin samples will be analysed at the carbon fiber length scale of ∼1 µm. Microscopic and spectroscopic examination will be done at the research group on *Electrochemical and Surface Engineering* (SURF) of the *Vrije Universiteit Brussel* (VUB). Scanning Electron Microscopy (SEM) as well as spectroscopic tools, such as Energy-Dispersive X-ray spectroscopy (EDX) and Auger Electron Spectroscopy (AES), will be used to analyze the ablation phenomena of the carbon fibers and to evaluate the degradation inside the material. By doing so, a multiscale analysis in macro-, meso−, and microscale is being performed giving information about the depth of pyrolysis and char layer. The thinning and erosion of the carbonic fibers is of high interest [8; 19] as this helps in identifying the depth of the ablation zone and the susceptibility of the fibers to oxidation.

4.3. *Data integration and ablation model validation*

Physico-chemical models and material response codes will be developed in parallel, which will address the thermo-chemistry of the pyrolysis gases (e.g. identification of the species produced), their transport in the porous material as well as their evolution in the boundary layer. This will be done by coupling flow solvers with material response codes, at first, in a 1D 'stagnation line' description with a moving mesh to account for the recession of the surface [20]. This approach will then be able to be extended to a 3D description.

The extracted experimental data will be employed for comparison of observable data with model estimates. In fact, the functional integration of both experimental and numerical data is essential to identify the properties, physical processes and other factors required to fully characterize the ablation phenomenon.

As an illustrative example we refer to the surface recession rate of an ablating material, which is the result of complex thermo-chemistry and gas-surface interaction. Well defined boundary conditions are required for an adequate numerical simulation, which are inferred from experimental observations of the quantity of interest. For example, the recession of the material is dependent on surface temperature and pressure which can be taken from specific experiments for a certain flow condition. The numerical model will then present species-densities and mass fraction distributions at the stagnation line of a simulated Plasmatron experiment on an ablative carbon-phenolic surface as well as the temperature distribution throughout the boundary layer. Such data is then able to be compared to experimentally estimated concentration gradients and temperatures in the boundary layer, identified by means of emission spectroscopy.

4.4. *Flight extrapolation*

Duplication of the real hypersonic reentry condition in a ground-test facility can be achieved under the Local Thermochemical Equilibrium (LTE) assumption if the flight total enthalpy H_f, the total pressure p_f and the velocity gradient at the wall β_f are locally matched on the test sample. To inversely extrapolate the real flight condition from experiments, different steps are performed based on the Local Heat Transfer Simulation (LHTS) concept (Fig. 6). This methodology was

developed at the Institute for Problems in Mechanics of Moscow (IPM)[21] and applied to the Plasmatron facility [22]:

At first, heat flux and pitot pressure are intrusively determined during the experiment. The next step consists of numerically simulating the plasma flow using a Navier-Stokes-Solver characterizing the boundary layer geometry around the test sample under LTE and axisymmetric flow assumption (VKI ICP code [23]). Finally, the VKI Boundary Layer Code [24] is solving the chemically-reacting stagnation line boundary layer over a catalytic surface (the intrusively used calorimeter) under non-equilibrium conditions. The

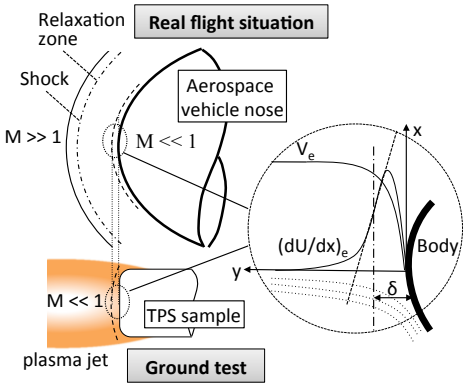

Figure 6: Local Heat Transfer Simulation (LHTS): Accurate duplication of the re-entry flight condition, existing at the stagnation point of an atmospheric entering vehicle, in a ground based plasma facility.

input boundary conditions for this tool are obtained from the experimentally determined heat flux and pitot pressure (step 1) as well as the so called five non-dimensional parameters (NDPs) coming from the flow solver (step 2). The code then iterates on the boundary layer outer edge temperature T_e, until experimental and numerical heat flux are matched, and provides outer edge enthalpy h_e and velocity v_e.

This procedure is up to now able to rebuild the freestream properties of the plasma jet and further, to extrapolate ground tests on reusable heat shields based on the principle of surface radiation to real flight conditions, such as for ceramic tiles and C-SiC compounds [25]. By flight conditions we mean a set of freestream conditions that will reproduce in the boundary layer of the space vehicle (near the stagnation point) the same kind of environment as found in the ground facility.

This methodology will be extended to ablative material testing with implementing new numerical models and validating them by means of comprehensive experiments. A complete analysis will be realized consisting of the plasma flow field, the reactive boundary layer (firstly in a stagnation line description), and brought to completion by coupling the decomposing material response. This will enable extrapolation of ground tests to real flight conditions, giving the material response of a specific material for selected points along the reentry trajectory. Such complex studies will allow for computation of the heat flux throughout the degrading material and, therefore, make TPS sizing possible.

5. Preliminary results on a carbon fiber preform

5.1. Atmospheric plasma tests

A low density, porous carbon fiber preform, obtained from Mersen Scottland Holytown LTD, was tested in the Plasmatron facility at sub-atmospheric conditions (15-200 mbar). The bulk carbon preform consists of 2D randomly oriented carbon fibers with their through-the-thickness (TTT) direction parallel to the flow direction. The fiber compound typically as a density of around 180 $\mathrm{kg/m^3}$, depending on the fabrication process and the nature of the precursor. The sample shape exposed to the flow was a flat faced cylinder of 45 mm length and 50 mm in diameter at a distance of 445 mm to the plasma-torch exit. Two type-K thermocouples were installed inside the sample at a distance of 10 mm and 20 mm downstream the initial stagnation point. Intrusively measured cold wall heat flux, surface temperatures as well as corresponding ablation quantities such as mass loss and recession are reported in Table 1.

Table 1: Test conditions (static pressure p_s, mean cold wall heat flux $\dot{q}_{cw}$) and comparison of surface temperatures at test end ($T_{S,end}$), mass loss ($\dot{m}$) and recession (r) in air plasma at a test time of 90 s.

p_s [mbar]	$\dot{q}_{cw}$ [$\mathrm{kW/m^2}$]	$T_{S,\,end}$ [K]	$\dot{m}$ [g/s]	r [mm]
(#1) 15	1021	2288	6.88/90	7.0
(#2) 100	946	1909	5.49/90	5.0
(#3) 200	1026	2228	5.11/90	5.5

The cold wall heat flux was constantly kept at 1 $\mathrm{MW/m^2}$ for the three test cases with static pressures in the test chamber varying between 15-200 mbar. Surface and internal temperature histories of low (#1) and high (#3) pressure case are presented in Fig. 7. A malfunction was recorded by thermocouple 10 mm /

15 mbar but is plotted for completeness. The internal temperatures still indicate material differences compared to a fully impregnated ablator, as both thermocouple outputs start rising quickly after sample injection. The protective endothermic pyrolysis processes of a fully compounded composite ablator would prevent penetration of the heat wave into the material.

For the flow conditions presented, the formation of CO due to atomic oxygen is expected to be the dominant reaction with the solid carbon of fibers (C_s). Reactions with nitrogen species as well as sublimation are neglected in this regime:

$$O + C_s \rightarrow CO \tag{1}$$

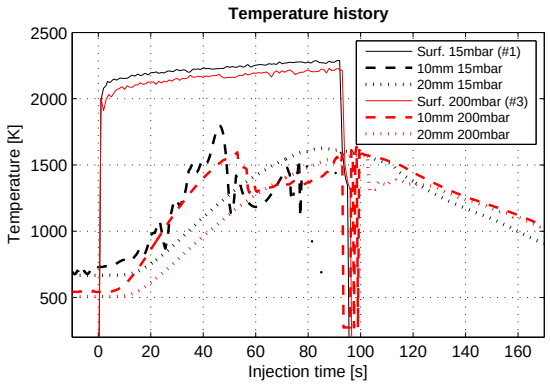

Figure 7: Surface and in-depth (10 mm & 20 mm from initial stagnation point) temperature history for carbon prefom ablation tests, mean surface temperature difference $\triangle\overline{T}$ = 70 K, thermocouples located 10 mm inside show malfunction (15 mbar) or break at T_{max} = 1500 K

However, the surface temperatures being in the order of 2200 K highly suggest a diffusion-controlled regime making surface kinetics insignificant [26]. In other words, the high thermal energy at the surface promotes total depletion of oxygen by oxidation and hence, reactions are only restricted by the ability of oxygen to diffuse through the boundary layer to the carbon surface.

The concentration change of atomic oxygen in the freestream for the various conditions can be found in Table 2, listing the boundary layer edge rebuilt values (free-stream enthalpy, density and oxygen concentrations, as well as the atomic oxygen diffusion coefficient (at edge temperature T_e), which will be discussed below. From this it can be seen that the freestream concentration of atomic oxygen for test #3 (200 mbar) exceeds that of test #1 (15 mbar) by a factor of almost 13 due to a strong density change (mass fractions are constant throughout the tests). Both recession and mass loss of test #1 at 15 mbar exceed that of test #3 (200mbar) by around 30%, as can be found in Table 1. This is somewhat counter-intuitive as a higher oxygen concentration would be assumed to lead to stronger oxidation mechanisms and, therefore, higher recession of the material.

Table 2: Boundary layer edge rebuilding: Free-stream enthalpy h_e, density ρ_e, atomic oxygen concentration c_O and atomic oxygen diffusion coefficient (at T_e) for each static pressure (p_s) condition.

	p_s [mbar]	h_e [MJ/kg]	ρ_e [kg/m^2]	c_O [mol/m^3]	$\mathcal{D}_O$ [m^2/s]
(#1)	15	22.65	0.6E-3	0.0087	0.52
(#2)	100	22.49	3.8E-3	0.0544	0.09
(#3)	200	20.42	7.9E-3	0.1121	0.04

A crucial period for tests of decomposing materials is the time during "start-up" of the facility, which is needed to operate the system to the target conditions. During this procedure, which contains adjustment of test gas, chamber pressure and heat flux, possible test specimens are hold on the injection mechanism close to the hot plasma flow. This is known to lead to additional errors in mass loss measurements as the hot environment can already lead to decomposition of phenolic compounds through pyrolysis. However, this not likely to be the case for the carbon preform as the bulk material is already fully carbonized. Furthermore, manufacturer specifications of thermal gravimetric analysis (TGA) claim that no considerable oxidation processes start below 770 K and that mass loss during a 6h analysis at 770 K resulted in only 0.35% mass loss. The thermal environment beside the plasma jet is not assumed to reach this temperatures, what can also be observed in Fig. 7 for the internal thermocouples. However, the internal temperatures of test #1 at 15 mbar exceed that of test #3 by around 140 K although the mean cold wall heat fluxes are almost identical.

In order to research into this problem we need to consider the carbon preform as a porous medium at microscale. In such a porous medium oxygen is able to diffuse into the deeper structure if its diffusivity is fast enough compared to oxidation reactions in the surface char layer. This is modeled by the Thiele number Φ, which is small if the diffusivity $\mathcal{D}$ is much

higher than the fiber reactivity k_f [m/s]:

$$\Phi = \frac{L}{\sqrt{\mathcal{D}_i / s_f k_f}} \tag{2}$$

with L being a characteristic length, e.g. the sample length and s_f the fiber volume surface [m^2/m^3]. Using Fick's law it is able to retrieve averaged species diffusion coefficients of a multi-component mixture for species i:

$$\mathcal{D}_i = \frac{1 - x_i}{\sum_{j \neq i} x_j / \mathscr{D}_{i,j}} \tag{3}$$

where $\mathscr{D}_{i,j}$ are the binary diffusion coefficients given by:

$$\mathscr{D}_{i,j} = \frac{3}{16} \sqrt{\frac{2\pi k_B T (m_i + m_j)}{m_i m_j}} \frac{k_B T}{p \Omega_{i,j}^{(1,1)}} \tag{4}$$

The atomic mass of the diffusing species i and j are m_i and m_j, k_B is the Boltzmann constant and $\Omega_{i,j}^{(1,1)}$ are the collision integrals at pressure p and temperature T, which can be computed from fitting expressions provided in ref. [27]. From Equation 4 we can see that at constant temperature but decreasing pressure the diffusivity will increase. This is also listed in Table 2, where the diffusion coefficient of oxygen based on the outer edge temperature T_e is given.

This brings us to the conclusion that in the case of low pressure, where diffusivity increases and atomic oxygen concentration decreases (leading to a lower fiber reactivity k_f), the Thiele number can decrease. As a consequence, oxygen would be able to penetrate deeper inside the material leading not only to ablation at the surface but also to degradation of fibers located further inside the material. This necessitates an examination of tested samples at microscale in order to be able to evaluate the degradation mechanisms of the carbon fibers, as presented in the following section.

5.2. Microscopic analysis

Virgin and tested carbon preform ablation samples were used to perform a microscale analysis by means of Scanning Electron Microscopy (SEM). Figure 8 presents micrographs of the virgin material exposing the carbon fibers at the surface of the test sample. Two glued fibers can be observed being indicative of an average fiber length of $l_f = 650\,\mu m$ and an average fiber diameter of $d_f = 6.5\,\mu m$.

Figure 9 presents ablated fibers at the preform surface after an ablation test at 100 mbar static pressure.

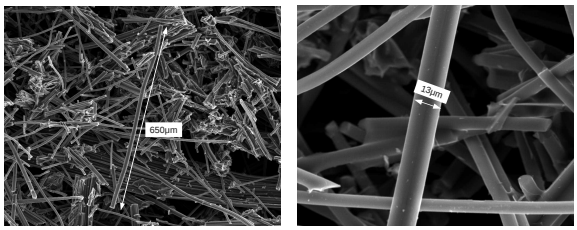

Figure 8: Surface of virgin carbon fiber preform showing two individual fibers glued together illustrating fiber length ($l_f = 650\,\mu m$) and doubled fiber diameter ($d_f = 6.5\,\mu m$).

On the first sight, a strong icicle shape of all fibers is visible due to their oxidation at the surface. It can also be said that the fibers shown in this micrographs are glued together to a fiber-bundle, which is a result of the manufacturing process of the preform. This leads to a certain percentage of all fibers being interconnected with a bunch of fibers to such bundles, embedded in between randomly oriented, individual carbon fibers. Several of such random fibers are shown in the micrograph to the right. Here, a thinning of the fiber is perfectly visible with the fiber diameter increasing from the top (inside the boundary layer) to the fiber-bottom (inside preform) reaching here almost the original fiber diameter of $d_f = 6.5\,\mu m$. A similar subject to thinning can be obs
This implies an oxidat
sure case of $\sim 250\,\mu m$

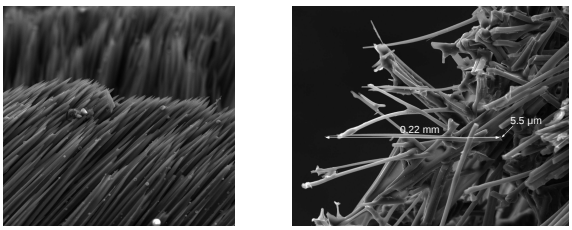

Figure 9: Ablated fibers at the preform surface (stagnation region, surface exposed frontal to the flow), thinning due to oxidation;
right: Fiber seems to be shortened due to ablation to a length of $\sim 220\,\mu m$ with its diameter increasing from fiber-top to fiber-bottom reaching almost the original fiber diameter of $d_f = 6.5\,\mu m$ $\rightarrow$ oxidation zone of $\sim 250\,\mu m$.

Comparing these results with micrographs taken after an ablation test at 15 mbar, reveals a few significant differences. Figure 10 presents such micrographs showing a fiber bundle at the surface of the preform being exposed to strong oxidation processes. However, compared to the micrographs shown before, a real icicle shape is not visible but rather strong degradation of the fibers over their whole length.

Such degradation in depth supports the assumptions

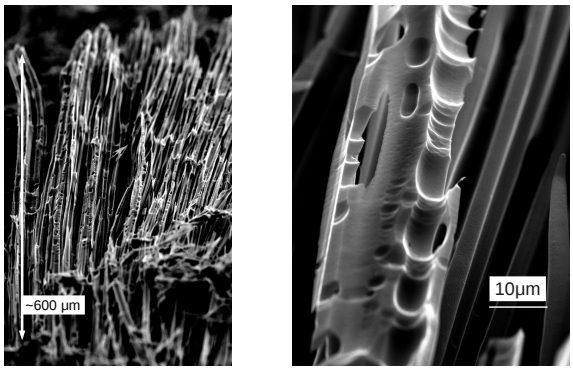

Figure 10: Fiber bundles exposed to the flow at the surface present strong corrosion of fibers throughout their whole length rather than a regular thinning from fiber-top to fiber-bottom.

found in the preceding section: A low pressure environment may lead to both increased oxygen diffusion along with decreased fiber reactivity, due to a lower oxygen concentration. With this, oxygen would be able to attack the fibers also in-depth rather than ablating only at the surface. This can weaken the substructure and for example lead to spallation, one mode of mechanical breakdown of the material, releasing small particles. Furthermore, fiber-bundels were identified in several micrographs of virgin but also ablated samples as mentioned before. As those bundles are embedded in-between individual fibers, they migh detach as soon as the surrounding fibers are ablated to a certain state, not able to retain a bundle anymore. Such mechanical failure could be the reason for an increased mass loss and recession of the material in various flow conditions.

An illustration of mechanical destruction of the material is given in Fig. 11, which shows two pictures taken by different instruments: A conventional reflex camera at comparable high exposure time (5 ms), exposing bright sparks during the ablation test, as well as a HSC image using a very short exposure time (5 µs). This reveals the flow being highly loaded with particles coming from the preform, what was constantly visible throughout the whole ablation test. This could be the result of what was said before: detaching fiber bundles as the preform ablates, releasing amounts of glued fibers at once to the flow, which then burn up in the hot plasma gas.

5.3. Comments

The preceding section briefly analyzed oxygen diffusion into the porous medium underlined by micrographs of ablated samples. However, although gas dynamics of the plasma flow are in continuum regime at

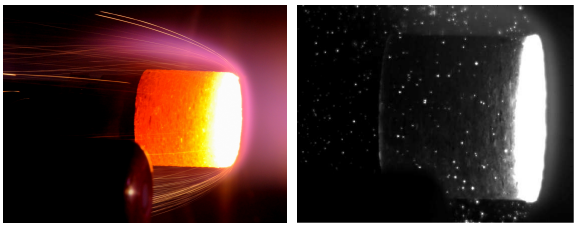

Figure 11: Images taken during a preform ablation test (p_s = 100 mbar); left: conventional picture taken with Nikon D5000, bright sparks visible (exposure time: 5 ms); right: taken with high speed camera, flow loaded with illuminated particles, probably assignable to spallation (exposure time: 5 µs)

the scale of the test sample, inside the porous preform the scale of interest is much smaller. Here, the Knudsen number is defined as the ratio of mean free path $\overline{\lambda}$ and pore diameter d_p:

$$Kn = \frac{\overline{\lambda}}{d_p} \tag{5}$$

Especially the fiber bundels, with a mean pore diameter of the order of 10 µm, a high Knudsen number of $Kn > 1$ can occur leading for low pressures to gas dynamics in the rarefied regime. This has to be kept in mind for any theoretical analysis of ablation in-depth of the material compared to pure surface ablation. Especially numerical models for mass transport at this small scale have to be adapted, e.g. using Boltzmann solvers as in the direct simulation Monte Carlo (DSMC), as the conventional macroscopic description using the Navier-Stokes equations is inappropriate in this regime.

6. Summary

The first part of this paper reviews the efforts undertaken at the VKI in ablation testing during the last years and concludes with an ablation testing strategy for future investigations of innovative low-density materials. This methodology will be followed to obtain crucial data for material response characterization, development and validation of new numerical models with final extension to real flight extrapolation.

The second part presents preliminary results of ablation experiments on a carbon fiber preform, which is the basic material for new class ablators before phenolic impregnation. The material was tested at a constant cold wall heat flux of 1 MW/m^2 with varying static pressures (15-200 mbar). A higher mass loss and recession of the sample was found at lower pressure level. SEM micrographs revealed strong degradation

of carbon fibers over their whole length (650 μm), especially for low static pressures. This raised the question in what extend oxygen is able to penetrate into the porous material. A first estimation of diffusion coefficients of atomic oxygen resulted in a rise of more than one order of magnitude from high (200 mbar) to low pressure (15 mbar) cases. More experiments along with numerical assistance are required to support those trends.

Acknowledgments

The authors are thankful to Mersen Scotland Holytow LTD for supplying the bulk carbon preform material. The research of B. Helber is funded by a Ph.D. grant of the Agency for Innovation by Science and Technology (IWT). Pascal Collins is acknowledged for his valuable help as Plasmatron operator.

References

[1] Sherman, M.M., NASA Space Vehicle Design Criteria, Entry Thermal Protection, NASA SP -8014, NASA Langley Research Center (1968).

[2] Pavlosky. J. E., Leger, L. G., Apollo Experience Report - Thermal Protection Subsystem, NASA TN D -7564 (1074).

[3] Kendall, R. M., An analysis of the coupled chemically reacting boundary layer and charring ablator: Part V, A General Approach to the Thermochemical Solution of Mixed Equilibrium-Nonequilibrium, Homogeneous or Heterogeneous Systems, NASA CR -1064 (1968).

[4] Milos, F. S., and Chen, Y.-K., Comprehensive model for multicomponent ablation thermochemistry, in: Aerospace Sciences Meeting & Exhibit, 35th, AIAA paper 1997-0141, Reno, NV, Jan. 1997.

[5] Tran, H. K., Johnson, C. E., Rasky, D. J., et al., Phenolic Impregnated Carbon Ablators (PICA) as Thermal Protection Systems for Discovery Missions, in: NASA, TM 110440, 1997.

[6] Tran H. K., Development of Lightweight Ceramic Ablators and Arc Jet Test Results, in: NASA TM-108798, Jan. 1994.

[7] Ritter, H., Portela, P., Keller, K., Bouilly, J. M., and Burnage, S., Development of a European Ablative Material for Heatshields of Sample Return Missions, in: 6th European Workshop on TPS and Hot structures, Stuttgart, Germany, 1-3 April 2009.

[8] Lachaud, J., Cozmuta, I., and Mansour, N. N., Multiscale approach to ablation modeling of phenolic impregnated carbon ablators, Journal of Spacecraft and Rockets 47 (6) (2010) 910–921.

[9] Torre, L., Kenny, J. M., and Maffezzoli, A. M., Degradation behaviour of a composite material for thermal protection systems Part I - Experimental characterization, Journal of Materials Science 33 (1998) 3137–3143.

[10] Cozmuta, I., Wright, M. J., and Willcockson, W. H., Defining Ablative Thermal Protection System Margins for Planetary Entry Vehicles, in: AIAA 2011-3757, 2011.

[11] Moyer, C. B., and Rindal, R. A., An analysis of the coupled chemically reacting boundary layer and charring ablator: Part II, Finite Difference Solution for the In-Depth Response of Charring Materials Considering Surface Chemical and Energy Balances, NASA CR 1061 (1968).

[12] Vancrayenest, B., and Fletcher, D. G., Investigation of the Thermochemistry of Ablation of Graphite for Planetary Entry Applications, in: AIAA 2005-5062, 2005.

[13] Vancrayenest, B., and Fletcher, D. G., Emission Spectroscopic Survey of Graphite Ablation in the VKI Plasmatron, in: AIAA 2006-2907, 2006.

[14] Vancrayenest, B., and Fletcher, D. G., Ablation of Carbonaceous Heatshields: Spectroscopic Emission Survey in a Subsonic ICP Flow, in: AIAA 2008-3911, 2008.

[15] Asma, C. O., Helber, B., Di Lello, L., Panerai, F., and Magin, T., Infrared thermography measurements on ablative thermal protection systems for interplanetary space vehicles, in: 10th Quantitative Infrared Thermography Conference, Quebec City, Canada, 2010.

[16] Helber, B., Asma, C. O., Babou, Y., Chazot, O. and Magin, T. E., Experimental Investigation of the Material Response of Carbon Composite Ablators in the VKI Plasmatron Facility, in: AIAA-2011-2302, 2011.

[17] Helber, B., Babou, Y., Panerai, F., Chazot, O., Hubin, A., and Magin, T. E., Investigation of the gas-surface interaction of innovative carbon composite ablators in the VKI Plasmatron, in: 7th European Aerothermodynamics Symposium, Brugge, Belgium, 9-12 May, 2011.

[18] Bottin, B., Chazot, O., Carbonaro, M., van der Haegen, V., Paris, S., The VKI Plasmatron Characteristics and Performance, in: RTO AVT Course on Measurement Techniques for High Enthalpy and Plasma Flows, published in RTO EN-8, Belgium, 1999.

[19] Lachaud, J., Mansour, N. N., Microscopic scale simulation of the ablation of fibrous materials, in: AIAA paper 2010-984, 2010.

[20] de Muelenaere, J., Lachaud, J., Mansour, N. N., and Magin, T. E., Stagnation line approximation for ablation thermochemistry, in: AIAA paper 2011-3616, 2011.

[21] Kolesnikov, A. F., Conditions of Simulation of Stagnation Point Heat Transfer from a High-enthalpy Flow, Fluid Dynamics 28 (1) (1993) 131–137.

[22] Barbante, P. F., and Chazot, O., Flight Extrapolation of Plasma Wind Tunnel Stagnation Region Floweld, Journal of Thermophysics and Heat Transfer 20 (3) (2006) 493–499.

[23] Degrez, G., Vanden Abeele, D. P., Barbante, P. F., and Bottin, B., Numerical Simulation of Inductively Coupled Plasma Flows under Chemical Non-equilibrium, International Journal of Numerical Methods for Heat and Fluid Flow 14 (4) (2004) 538–558.

[24] Barbante, P. F., Degrez, G., and Sarma, G. S. R., Computation of Nonequilibrium High Temperature Axisymmetric Boundary-Layer Flows, Journal of Thermophysics and Heat Transfer 16 (4) (2002) 490–497.

[25] Panerai, F., Aerothermochemistry Testing of Thermal Protection Systems, Ph.D. thesis, von Karman Institute for Fluid Dynamics / University of Perugia (2012).

[26] Park C., Effects of Atomic Oxygen on Graphite Ablation, AIAA Journal 14 (11) (1976) 1640–1642.

[27] Capitelli, M., Gorse, C., Longo, S., and Giordano, D., Collision Integrals of High-Temperature Air Species, Journal of Thermophysics and Heat Transfer 14 (2) (2000) 259–268.

Modeling of Inductively Coupled Plasma Reactor for Nanoparticles Production

Silvânia Lopes

Aeronautics and Aerospace Department, von Karman Institute for Fluid Dynamics, Belgium, lopes@vki.ac.be

Supervisor: Patrick Rambaud

Associate Professor, Aeronautics and Aerospace Department, von Karman Institute for Fluid Dynamics, Belgium, rambaud@vki.ac.be

University Supervisor: Jean-Marie Buchlin

Professor, Université Libre de Bruxelles, Belgium, buchlin@ulb.ac.be

Abstract

The general purpose of this thesis is to design an inductively coupled plasma (ICP) reactor for efficient production of nanoparticles at industrial scale. In the present work, a mathematical model has been developed for simulating the formation of nanoparticles in an ICP reactor. The model describes the evolution of the particle size distribution accounting for particle nucleation and growth by condensation and coagulation, using the method of moments. The effects of the quenching mechanism on the temperature fields and on the formation of the nanoparticles is investigated. The results show that the cooling efficiency has a strong impact on the final particle size.

Keywords: ICP plasmas, nanoparticles synthesis, CFD modeling

Nomenclature

d_1	Atomic size of the particle (m)
d_m	Particle mass diameter(m)
m_1	Mass of the atom
D_j	Diffusion coefficient of particle of size j
j	The size of the particle
j^*	Critical nucleus size
k_B	Boltzmann constant
m	Mass of particle
M_k	Moments of order k^{th}
n	Concentration of particle (m^{-3})
n_0	Initial concentration of monomers (m^{-3})
n_s	Vapor concentration at saturation (m^{-3})
S	Supersaturation ratio
T	Temperature
$\vec{u}$	flow velocity
w_1	Initial metal vapor concentration (m^{-3})
μ	Flow viscosity
λ	Mean free path
ρ	Density
Θ	Dimensionless surface energy
$slpm$	standard liter per minute

1. Introduction

Nanotechnologies, especially nanoparticles related applications, have recently received tremendous interest due to the great innovative potential they offer. Nanomaterials are usually produced by compaction of nanoparticles powder. They are characterized by a larger number of grain boundary interfaces in which the local atomic arrangements are different from those of the crystal lattice [1]. The small size of the nanoparticles is also responsible for many changes in the thermo-physical properties compared with the bulk materials, which makes them suitable for novel applications. Examples of these new properties include lower melting temperature, improved hardness and ductility, high self-diffusion coefficient, catalytic activity, and intriguing optical and electronic properties. However, the processes used to generate those nanoparticles play an important role in terms of particles size, morphology, crystalline phase and composition, which fundamentally determine the properties of the nanostructure material.

Thermal plasma processing, and in particular

high-frequency inductively coupled thermal plasmas (ICTP), have shown several distinctive advantages over other synthesis routes for nanoparticles. Due mainly to its high temperature and energy density, as well as the large plasma volume and long residence/reaction time, it is considered relatively easy, in principle, to evaporate all injected micro particles and then to quench and condensate the vapors to obtain the desired nanoparticles [2]. Additionally, an ICTP is generated without any internal electrodes and therefore inherently free of contamination and it offers the possibility to work under a controlled atmosphere.

In spite of all these advantages related to ICTP, neither the precise control of the particle size, distribution and morphology nor mass production has be successfully achieved in practice. The effects of t plasma torch and quenching parameters, including actor design and configuration, on the flow field a on the formation of the nanoparticles appear to be enormous importance [3].

Modeling studies can play an important role in t development and improvement of the nanopartic synthesis processes, providing an insight into the pl nomena involved and helping to identify the right c erating conditions to employ. However, a full theor ical description of particles dynamics in plasma flo within an actual industrial environment is very co plex. A complete model of such a system requires t solution of the fluid mechanics equations of contir ity, momentum and energy, coupled with the electi magnetic field equations, which describe the gene tion of the plasma flow; with the description of r cro particles evaporation in plasma flow; and with t aerosol dynamics equations, describing the nanopar cles formation. Nanoparticles are formed by num ous coexisting mechanisms, such as nucleation, co densation, coagulation, surface reaction, and coal cence or sintering. Several methods have been dev oped to represent the evolution of a population of p ticles, droplets or bubbles in a flow fields. These pop lation balance methods often use statistical techniq based on moments of distribution. Among these me ods of moments, the method developed by Frenkla [4] (MOMIC-Method of Moments with Interpolati Closure) has been one of the most used to repres the evolution of nanoparticle from a vapor phase. It remains still a simple, effective and easy method to implement. It can be used in a system within presence of nucleation, Brownian coagulation, condensation, thermophoresis, chemical reactions and aggregates which allows to describe the morphology of the powders produced.

In the previous study, an extended-field Computational Fluid Dynamic (CFD) model for simulating the behavior of inductively coupled plasma torches (ICPTS) had been implemented using the open source code, OpenFOAM. The model has been used to study the effects of operating conditions and torch design on the velocity and temperature fields in the ICP torch. Moreover, estimations of the particle residence time and accumulative heat for the different operating conditions has been done to evaluate the best conditions for particle evaporation. In this study, the plasma CFD model has been partially coupled with the nanoparticles model, which describes the formation of nanoparticles from a plasma vapor flow. The model is applied

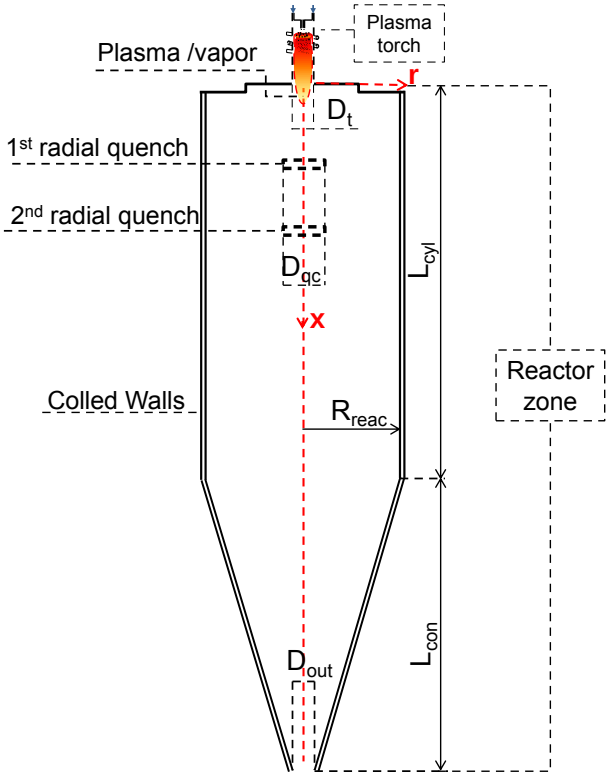

Figure 1: Schematic of the ICP plasma reactor

2. Model description

Up to this point, the overall model developed to optimize ICP reactor design consists of two parts. The

first part concerns the modeling and design of inductive argon plasma, used for synthesis of the nanoparticles. It essentially presents the fluid dynamics of the plasma flow in the presence of an electromagnetic field. Since on this work we focus on the nucleation and growth of metal vapor, the plasma flow itself is not included in the analysis. The second part deals with the formation of nanoparticles accounting for nucleation and growth by coagulation of the metal vapor in the reactor zone, considering different mechanisms of transport.

2.1. Nanoparticle Model

In the reactor zone, the metal vapor created in the plasma zone is quenched and converted in nanoparticles. To describe this phenomenon several assumptions are introduced:

- instantaneous homogeneous nucleation,
- the particles follow the fluid flow,
- the particles are spherical,
- Brownian coagulation in free molecular regime, because of the small size of the particles,
- nanoparticle size with a log-normal distribution,
- the only growth mechanism is coagulation.

The particle size distribution functions (PSDFs) of nanoparticles are obtainable by solving the general dynamic equation for aerosol growth (Eq. 1), taking into account the contribution of the different mechanisms (nucleation, coagulation, thermophoresis and diffusion).

$$\vec{\nabla}\cdot(\vec{u}n_j) = \overbrace{-\vec{\nabla}\cdot(\vec{u}_{th}n_j)}^{thermophoresis} + \overbrace{\vec{\nabla}\cdot(D_j\nabla n_j)}^{diffusion} + \overbrace{I j^{*}\delta_{j-j^{*}}}^{nucleation} + \underbrace{\frac{1}{2}\sum_{i=j^{*}}^{j-1}\beta_{i,j-1}n_i n_{j-1} - n_j\sum_{i=j^{*}}^{\infty}\beta_{i,j}n_i}_{coagulation} \quad (1)$$

2.1.1. Particle nucleation

According to the classical theory [5], homogeneous nucleation is the formation of particles from a supersaturated vapor, which is caused by the fast cooling of the gas. For the present model, the nucleation rate is given by the expression developed by Girshick [6]:

$$I = \frac{\beta_{11}n_s^2 S}{12}\sqrt{\frac{\Theta}{2\pi}}\left(\Theta - \frac{4\Theta^3}{27ln^2 S}\right) \quad (2)$$

where S is the supersaturation pressure, β_{11} is the Brownian coagulation coefficient between two manometers and Θ the dimensionless surface energy.

2.1.2. Particle Growth-Coagulation

Coagulation is the interparticle phenomenon wherein nanoparticles collide with one another, due to a relative motion between them and adhere to form a larger particle. After the instantaneous nucleation, the particles coalesce due to the brownian movement. Because most of the particles are smaller than the mean free path, the typical Knudsen numbers vary between 20 and 2000; therefore the Brownian motion is assumed in free molecular regime. It is characterized by $Kn >> 1$; in this case, the frequency of collision is expressed by the following expression presented by Frenklach [4]:

$$\beta_{i,j} = 2.2\sqrt{\frac{6k_BT}{4\rho}}\left(\frac{3m_1}{4\pi\rho}\right)^{\frac{1}{6}}\sqrt{\frac{1}{m_i}+\frac{1}{m_j}}\left(m_i^{\frac{1}{3}}+m_j^{\frac{1}{3}}\right)^2 \quad (3)$$

2.1.3. Thermophoresis

This phenomenon appears as a result of the gradient of temperature experienced by the particles in flow [5]. The thermophoresis velocity is independent of the particle size in the free molecular regime and is represented by:

$$\vec{u_{th}} = -\frac{0.55\mu}{\rho T}\vec{\nabla}T \quad (4)$$

2.1.4. Brownian Diffusion

In case of small particles flowing in the high temperature zones of the rector, the Brownian motion becomes important. The diffusion coefficient of particle of size d_j is then given by [7]:

$$D_j = \frac{k_BT}{3\pi\mu d_j}\left(1+\frac{3.31\lambda}{d_j}\right) \quad (5)$$

2.2. Method of Moment

It is generally difficult to solve Eq. 1 because of its nonlinearity. The method of moment reformulates the problem into a small set of differential equations describing the evolution of the moments of the PSDFs.

The *kth* moment M_k is defined as

$$M_k = \frac{1}{\rho n_0}\sum_{i=j^{*}}^{\infty} j^k n_j \qquad (k = 0, 1, 2, ...) \quad (6)$$

The moments of the size distribution are normalized with respect to the density ρ and the initial monomers concentration n_0 at the entrance of the reactor. The moments M of order 0 and 1 are the number concentration and mass of the particles in a given volume, respectively. The moment of order 2 is also known to be proportional to the light scattering by the nanoparticles when they have much smaller size than the wavelength of the incident light. Therefore, the definition of the moments of size distribution leads to the formulation of conservation equations (Eq. 1) in terms of moments (Eq. 7)

$$\frac{\partial(\rho M_k)}{\partial t} + \vec{\nabla}\cdot(\rho\vec{u}M_k) = -\vec{\nabla}\cdot(\rho\vec{u_{th}}M_k) + \vec{\nabla}\cdot(\rho\overline{D}\vec{\nabla}M_k) + \underbrace{\frac{I}{n_0}(j^*)^k}_{nucleation} + \underbrace{\frac{\rho^2 n_0}{4}\left[k^2+k-2\right]\Phi_{0,0}M_{k/2}^2}_{coagulation} \quad (7)$$

These conservation equations can be solved with the flow equation to describe the spatial distribution of the moments in the flow field.

The conservation of manometer in vapor phase is obtained by the mass balance over the aerosol and the vapor, as follow:

$$\frac{\partial(\rho\omega_1)}{\partial t} + \vec{\nabla}\cdot(\rho\vec{u}\omega_1) = \vec{\nabla}\cdot(\rho D_1\vec{\nabla}\omega_1) - Ij^*m_1 \quad (8)$$

For the moments of order k the contribution of nucleation and coagulation can be obtained directly by:

$$\frac{d(\rho M_k)}{dt}(nucl) = \frac{I}{n_0}(j^*)^k \quad (9)$$

and

$$\frac{d(\rho M_0)}{dt}(coag) = -\frac{\rho^2 n_0}{2}\phi_{0,0}M_0^2 \quad (10)$$

$$\frac{d(\rho M_1)}{dt}(coag) = 0 \quad (11)$$

$$\frac{d(\rho M_2)}{dt}(coag) = \rho^2 n_0 2\phi_{0,0}M_0^2 \quad (12)$$

In this study, the moment method is used for the first three moments of the PSDF. Using the hypothesis of log-normal particle size distribution, it is possible to calculate the different moments of the particle size distribution in a close form using only the first three moments of distribution. The collision coefficient $\phi_{0,0}$ is estimated by logarithmic interpolation of the reduced moments $\mu = M_r/M_0$ of fractional order. This method was proposed by Frenlach and Harris and it is detailed in Refs [4] [8].

Total concentration	M_0
Mass of particles	M_1
Mass diameter	$d_1 M_{1/3}/M_0$
Mean surface	$s_1 M_{2/3}/M_0$
Mean volume	$v_1 M_1/M_0$

Table 1: Principal physical properties of PSDFs

The principal physical properties of the PSDF (mass mean diameter, standard deviation) are obtained from the moments distributions, as defined on table 1 [5]. Therefore, a closed system of equation can be obtained to describe the evolution of the moments distribution in function of its own properties.

3. Model implementation

3.1. Reactor geometry and initial conditions

The nanoparticle model is applied to the reactor illustrated in Fig. 1 with the quenching mechanism. This ICP reactor has been developed in the von Karman Institute for nanoparticles production at industrial scale. The model is used to study the importance of the quenching on the final size of the particles. The quenching system consist of two quenching units, positioned perpendicularly to the plasma jet axis. This quench design type has been also simulated by [9]. The geometry is considered as 2D axisymmetric, specified as a wedge of a 5 degree angle and one cell thickness along the plane of symmetry (Fig. 2). The quenching inlet is therefore a uniform slot (which

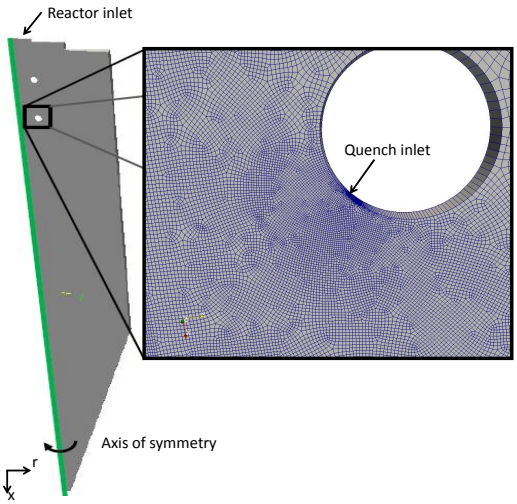

Figure 2: Axisymmetric geometry and reactor mesh.

corresponds to an annular injection around the quench

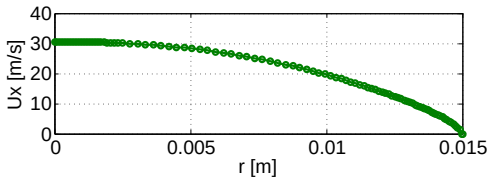

(a) Axial velocity

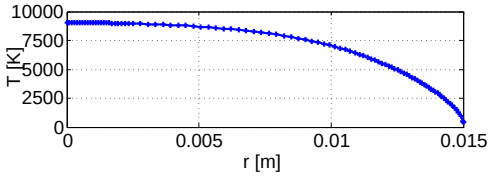

(b) Temperature

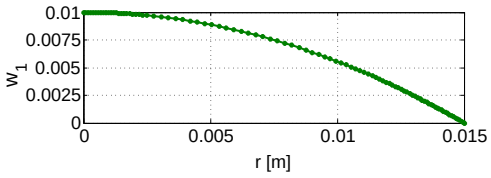

(c) vapor concentration

Figure 3: Inlet profiles at the entrance of the reactor.

unit) of equivalent diameter of the real radial quench inlets. The positions of the first and second quench units, and its respective intensity and injection angle had been previously study in order to determine the better conditions for fast cooling without a large perturbation of the flow.

In all the cases studied, the profiles at the entrance of the reactor are from the exit conditions of the inductive plasma torch solution for $5kW$ of dissipated power, $0.96g/s$ of argon mass flow and 1% of metal vapor (Fig. 3).

3.2. Simulations

Before analyzing the effects of the quench design on the nanoparticles formation, some numerical parameters has been investigated to obtain satisfactory convergence and stability. The grid size dependency has been analyzed, together with different numerical schemes and solver controls. The k-Omega SST and k-Epsilon models have been also implemented and analyzed for the expansion of the plasma jet into the reactor zone. The results obtained show that the k-Omega SST is more suitable, predicting satisfactory behavior for the plasma jet. In contrast, with the k-Epsilon models the plasma jet suddenly extinguishes after entering the reactor, as can be seen in Fig. 4.

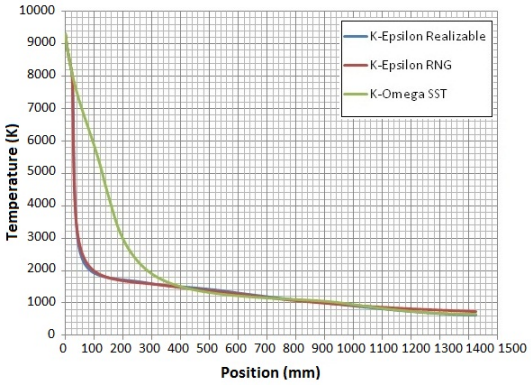

Figure 4: Static Temperature along the Axis for different turbulence models

The presence of strong turbulence in the particle formation zone is expected to affect the transport of the vapor and thus the trajectories of the nanoparticles. Shigeta and Nishiyama [10] have reported that turbulence must be accounted for even for relatively small overall Reynolds numbers. The plasma jet flame is often wavering and unstable accompanied with drastic heat/species transfer.

The gas flow temperature, velocity and concentration fields, together with the moments equations are then solved, in the reactor zone, assuming steady state, in turbulence regime modeled by k-Omega SST model and at atmospheric pressure. Thereafter, the effects of quenching rate, number position and angle are investigated.

4. Results and Discussion

Three different design conditions are presented. In the first case the reactor (No Quench) does not have any quench, only cold walls in the rector zone. In the second case (1 Quench) only one quench unity is considered, positioned at $95mm$ from the the reactor entrance, with 35 slpm of argon quenching gas injected with $45°$. The third reactor (2 Quench) uses a second similar quench units with $100mm$ distance from the first one and with 30 slpm of argon quenching gas. Figure 5 presents the temperature and the axial velocity contours for the three cases. As can be seen, the presence of the quenching units not only determines the cooling of the plasma jet but also has a strong effect on the flow trajectory, and therefore on the diffusion of the vapor in the reactor (Figure 7). The introduction of the first quench unit creates a shielded

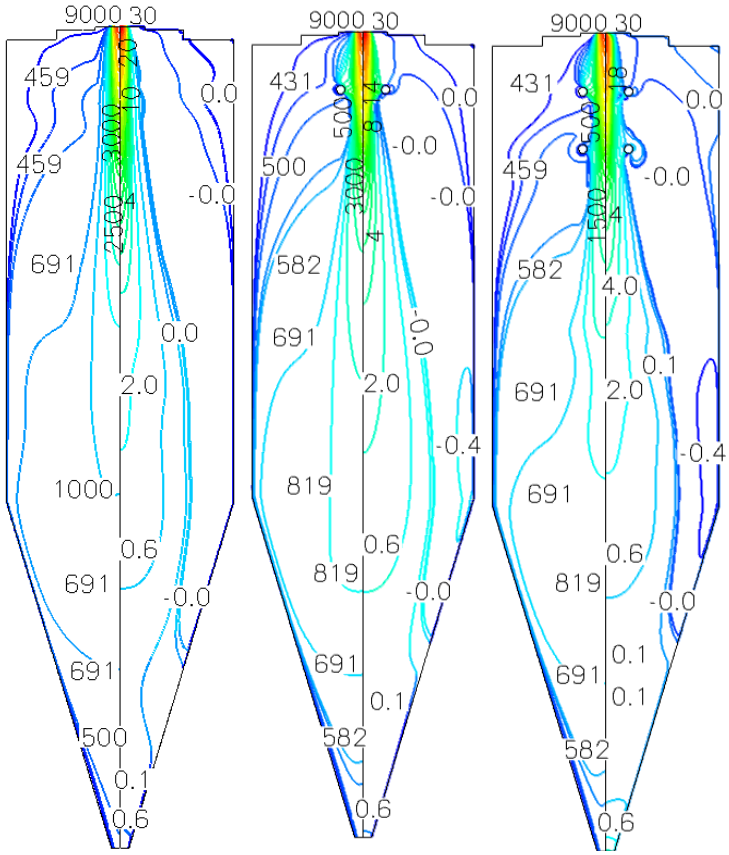

(a) No Quench (b) 1st Quench (c) 2nd Quench

Figure 5: Temperature contours [K] (left); Axial velocity [m/s] (right)

zone, keeping the vapor at the center of the reactor and favoring the stabilization of the flow. On the other hand, the second quench increases the cooling rate but also creates a small recirculation zone around its location. Fig. 6 shows the effects of the quench on the temperature fields in the reactor by plotting the axial profile of temperature at center line and the radial profile at $x = 0.4m$ for the cases of no quench, one stage and two stage quench, respectively. As expected, the injection of gas strongly affects the the temperature field by promoting a fast cooling of the flow. The concentration of vapor is reduced when the nucleation begins and also by dilution in case of quench injection. The temperature field and the vapor concentration indicate where the particles are formed or nucleation occurs. The temperature fields in the reactor establish the vapor pressure which influences the nucleation rate and strongly determines the coagulation and the thermophoresis terms.

Figure 8 shows the contours of the mean mass diameter with the concentration of particles for the three cases. The mean mass diameter is a physical property of PSDF in terms of moments, given by $d_m = d_1(M_{4/3}/M_0)$. Where d_1 is the atomic size of the particle, $M_{4/3}$ and M_0 are calculated moments. After the nucleation, the primary particles continue to grow due to the coagulation process. The effects of the quench design on the average mass diameter and particle concentration at the exit of the reactor can be seen in Fig. 8. The fast cooling introduced by the quenching units causes a decrease of the exit mean diameter. In case of no quench, large particles are formed near the walls ($\approx 50nm$) and the amount of formed particles is therefore lower. These results confirm the strong influence of quench design on the control of the particle size distribution. Similar results have been achieved by [7], [10] and [9], showing the dependence of the final particle size on the applied quenching.

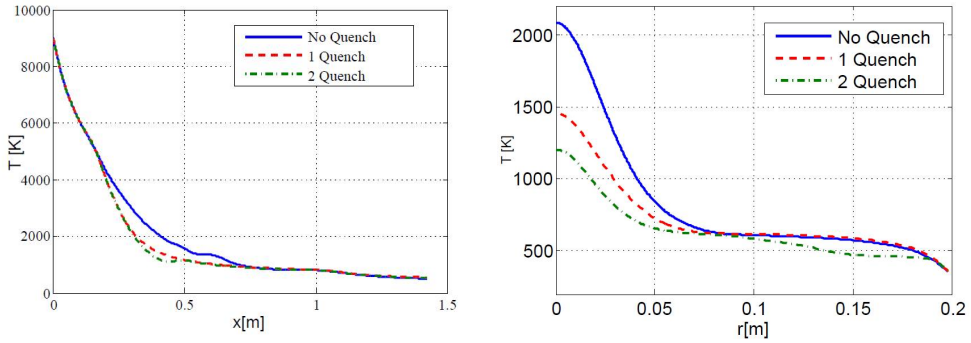

(a) at r= 0m (b) at x= 0.4m

Figure 6: Axial and radial temperature profiles

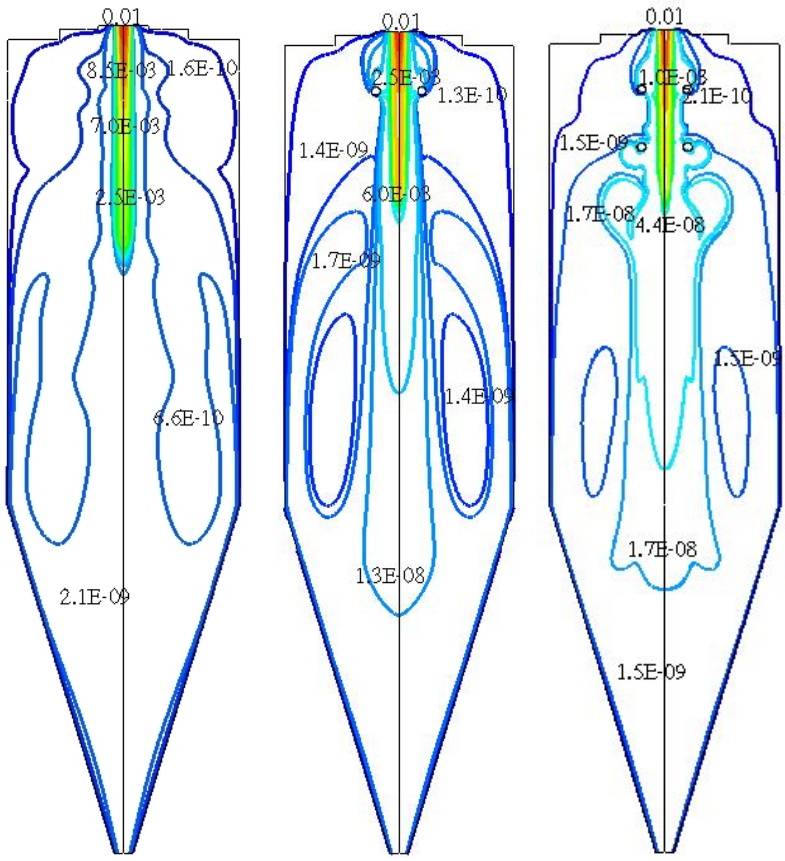

(a) No Quench (b) 1st Quench (c) 2nd Quench

Figure 7: Vapor mass fraction contours

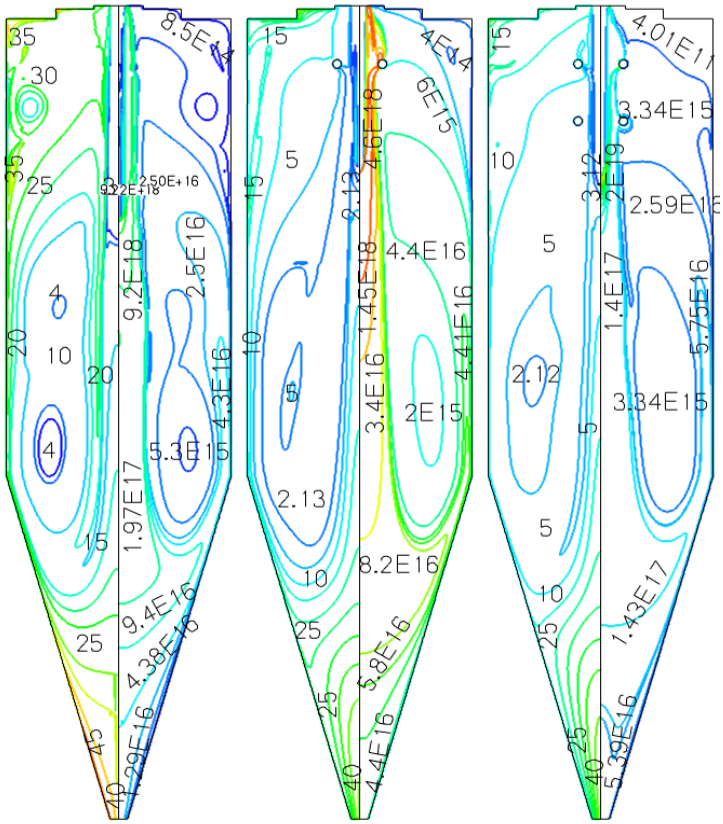

(a) No Quench (b) 1st Quench (c) 2nd Quench

Figure 8: Left: Average Mass Diameter [nm]; Right: Concentration of particles [m^{-3}]

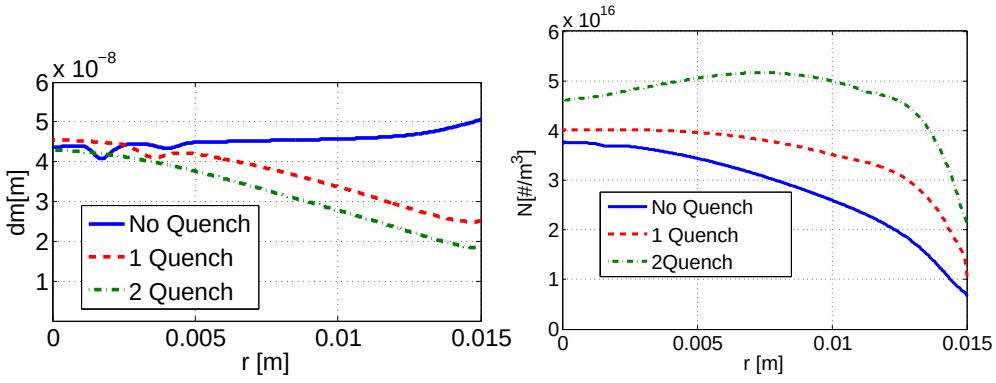

(a) Average Mass Diameter (m) (b) Concentration of particles (m^{-3})

Figure 9: Effects of the quench units at the exit of the reactor

5. Conclusion

The mathematical model was developed to simulate the formation of nanoparticles in an ICTP reactor. The model can be applied to study the importance of many parameters on the size distribution of the particles and morphology. In this present work, numerical investigation using the model was conducted to clarify the effects of the quenching flow. The results show that the quench strongly affects the temperature distribution in the reactor and consequently has a decisive impact on the final particle size. The diameters obtained at the exit of the reactor are between 40 and 50nm for the case without quench, 23 and 45nm using one quench unit and between 12 and 45nm using the double quench unit. This present model is limited to particles in free molecular regime and to nucleation and coagulation mechanism of growth. As reported by [7], the final size diameter does not change from considering only coagulation growth process. Although the condensation mechanism seems to have a dominant contribution in the growth, the overall growth mechanism is balanced.

The further extension of the model will include the condensation mechanism of growth, as well as a solid particle aggregation model. Different quench positions, intensities and injection angles will be also investigated in order to optimize the reactor design and the controlling of the final particle size.

Acknowledgments

I would like to thank my supervisor Patrick Rambaud, professor Pierre Proulx from the university of Sherbrooke and all the VKI NanoParticle project group for their help and support on this project. This work is supported by the Region Wallonne.

References

[1] S. L. Girshick, C. P. Chiu, R. Muno, C. Y. Wu, L. yang, S. Singh, P. McMurry, Thermal plasma synthesis of ultrafine iron particles, J. Aerosol Sci. vol. 24, No 3 (1993) pp– 367–382.

[2] E. Pfender, Y. C. Lee, Particle dynamic and particle heat and mass transfer in thermal plasmas. part i. the motion of a single particle without thermal effects, Plasma Chemistry and Plama Processing Vol.5, No 3 (1985) pp.211–237.

[3] N. Mendoza-Gonzalez, B. Goortani, P. Proulx, Numerical simulation of silica nanoparticles production in an rf plasma reactor: Effect of quench, Materials Science and Engineering C vol.27 (2007) pp.12651269.

[4] M. Frenklach, Method of moments with interpolative closure, Chemical Engineering science 57 (2002) 2229–2239.

[5] W. C. Hinds, Aerosol Techology, Wiley, 1999.

[6] S. L. Girshick, C. P. Chiu, Kinetic nucleation theory: A new expression for the rate of nucleation from an ideal supersatureted vapor, J. Chem. Phys. 93 (1990) 1273–1277.

[7] N. Mendoza-Gonzalez, M. E. Morsli, P. Proulx, Production of nanoparticles in thermal plasmas: A model including evaporation, nucleation, condensation and fractal aggregation, Journal of Thermal Spray Technology 17(4) (2008) 533–550.

[8] P. Proulx, J.-F. Bilodeau, A model for ultrafine powder production in a plasma reactor, Plasma Chemistry and Plama Processing vol.11 No 3 (1991) 371–385.

[9] C. Schreuders, Syntèse par plasma inductif de nanometriques de silicium optimization de la trempe, Ph.D. thesis, Universite de Limonges (2006).

[10] M. Shigeta, H. Nishiyama, Numerical analysis of metallic nanoparticle synthesis using rf inductively coupled plasma, Journal of Heat transfer - Transactions of the ASME vol.127 (November 2005) pp.1222–1229.

Ground Testing Methodologies Improvement in Plasma Wind Tunnels using Optical Emission Diagnostics

Alessio Cipullo

Aeronautics and Aerospace Department, von Karman Institute for Fluid Dynamics, Belgium, alessio.cipullo@vki.ac.be/alessio.cipullo@unina2.it

Supervisor: Olivier Chazot

Associate Professor, Aeronautics and Aerospace Department, von Karman Institute for Fluid Dynamics, Belgium, chazot@vki.ac.be

CIRA Supervisor: Federico De Filippis

Senior Research Engineer, Thermo-Structures Design and Experiments Department, CIRA, Italy, f.defilippis@cira.it

University Supervisor: Luigi Zeni

Professor, Information Engineering Department, Second University of Naples, Italy, luigi.zeni@unina2.it

Abstract

The characterization of the flow produced by CIRA SCIROCCO and VKI Plasmatron plasma wind tunnels was performed. The peculiar features of the two plasmas were addressed using optical emission spectroscopy, photomultiplier spectroscopy and high speed camera imaging. The temperature and total enthalpy were measured and compared to results from traditional diagnostics. Finally, the critical aspects and future perspectives are discussed.

Keywords: plasma, arc-jet, ICP, optical emission spectroscopy, photomultiplier spectroscopy, high speed camera imaging

1. Introduction

The development of new aerospace vehicles for future planetary exploration is a challenging task and involves a wide range of scientific and industrial expertise. One of the most important aspects is the appropriate design and implementation of Thermal Protection Systems (TPS). In this framework, the accurate reproduction of atmospheric entry phenomena in ground facilities for testing purposes is imperative. Nowadays, different technologies exist to produce plasma flows suitable for aerothermodynamic testings of TPS and the most popular are arc-jet wind tunnels and inductive coupled plasma (ICP) torches [1]. The technology adopted to get the plasma discharge is the key feature and it heavily influences the plasma flow aerothermochemistry. In arc-jets, the gas mixture is heated up by means of a DC discharge between two electrodes. Corrosion phenomena of the electrodes inner surface can introduce impurities in the flow. In ICPs, the gas is heated up by Joule effect inside a quartz tube, where a RF cylindrical discharge is generated. Because of the electrodeless design, the plasma is characterized by high purity. However, the power supply technology can be a source of undesirable unsteady heat and mass transfer phenomena in the flow.

The present work focuses on the experimental investigation of the flow produced by the two major European plasma facilities: SCIROCCO [2], [3] and Plasmatron [4], [5]. The first is a 70 MW arc-jet plasma wind tunnel and it is located at the Italian Aerospace Research Center (CIRA), the second is a 1.2 MW ICP torch and it is located at the von Karman Institute (VKI) for fluid dynamics. The peculiar features of the two types of plasma were addressed using optical emission diagnostics. In particular, Optical Emission Spectroscopy (OES) and Photomulti-

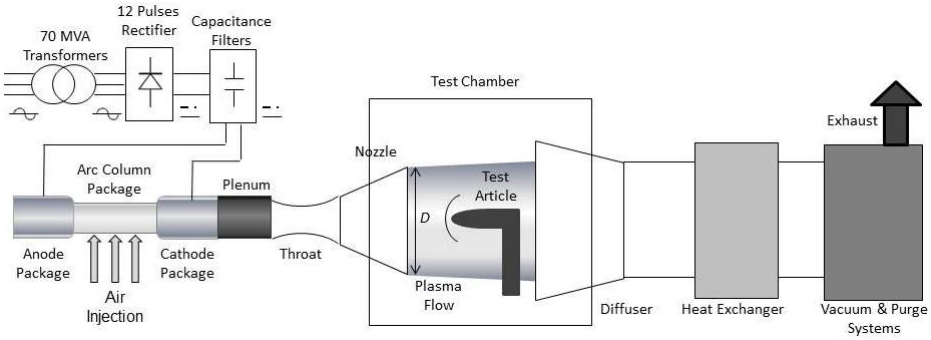

Figure 1: Simplified scheme of the CIRA SCIROCCO plasma wind tunnel with nozzle exit section diameter D=1150 mm. Side View.

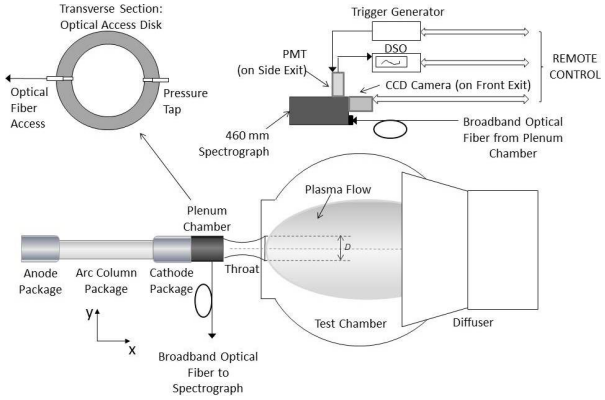

Figure 2: Simplified scheme of the experimental set-up for the CIRA SCIROCCO plasma wind tunnel (AURORA configuration, D=187 mm). View from the top.

plier Tube (PMT) spectroscopy were applied in the CIRA SCIROCCO plenum chamber for a set of conditions between 14.6 MW and 31.4 MW input electrical power. High Speed Camera (HSC) imaging and OES were applied to the VKI Plasmatron free-stream flow for a set of input electrical power between 120 kW and 300 kW. The above mentioned optical diagnostics were coupled to intrusive diagnostics in both cases. The final aim of the work is to investigate the total enthalpy determination methodologies in the two facilities.

Section II is dedicated to the experimental set-up. The description of the applied elaboration procedures is undertaken in section III. The experimental results are presented in section IV. The last part is dedicated to conclusions and future perspectives.

2. Experimental Set-up

2.1. CIRA SCIROCCO

SCIROCCO is the biggest and most powerful segmented constrictor type arc-jet facility worldwide. It uses a 70 MW DC power supply to ignite and sustain the electric arc into its 5500 mm long constricted-arc heater, between the anode and cathode packages (see Fig. 1). The constrictor internal diameter is 110 mm. The DC power is obtained through a cascade of high power transformers and a 12 pulses rectifier, fed by a dedicated high voltage AC line (50 Hz). After the rectification stage, a set of capacitance filters are used to smooth the conversion ripple. The nominal levels for DC voltage and current are V=30 kV and I=9000 A respectively. The cold gas mixture, made up of air and argon, is injected in the arc column in distributed locations using a swirling pattern. The maximum air mass flow rate is m_{air}=3.5 kg/s and the total pressure in the arc heater can reach P_0=17 bar. The gas is heated up by the arc and expanded through the nozzle. It then enters an evacuated test chamber, where the test article is placed. The nozzle exit diameter can be changed between D=187 mm and D=1950 mm, according to five different configurations. For the considered set of test conditions, two exit diameters were used: D=187 mm (AURORA configuration, where only the throat section is installed) and D=1150 mm. The pressure in the chamber is typically set to 0.10 mbar. The nominal flow Mach number is 12. Hot gas exits through a 50 m long diffuser and is cooled down by an active heat exchanger, before going to the 80 MW vacuum system and the purge unit to remove polluting products (such as NO_x). Although the nominal mass-averaged total enthalpy is H_0=45 MJ/kg, for typical test conditions H_0 is usually below 20 MJ/kg. Further details about SCIROCCO can be found in [2] and [3].

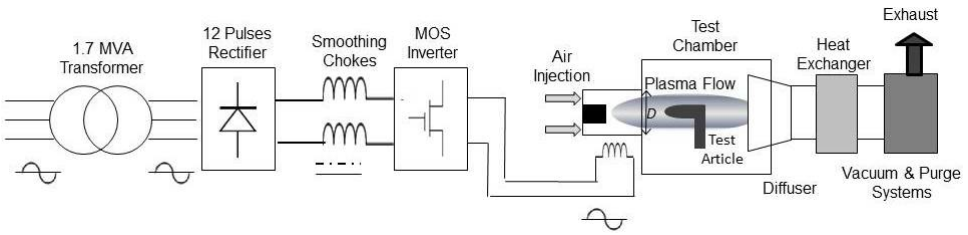

Figure 3: Simplified scheme of the VKI Plasmatron plasma wind tunnel with nozzle exit section diameter D=160 mm. Side View.

The experimental set-up is described in Fig. 2. The OES was performed using a silica optical fiber (200-1000 nm) looking directly at the internal part of the plenum chamber through an SMA connector and an integrated quartz window. The optical access disk is placed ~ 180 mm upstream the throat inlet section and its internal diameter is 172 mm. The diameter of the fiber core was 600 μm and the numerical aperture was 0.22 ± 0.02. The optical fiber was chosen to maximize the collected light intensity from the plasma. The light from the plasma was brought to the front entrance of a Jobin-Yvon HR460 spectrograph, having a focal length of 460 mm and a grating resolution of 1200 groves/mm. Spectral components were recorded using a Symphony CCD camera placed at the spectrograph front exit. It was characterized by a 1024×256 pixel matrix (with pixel dimensions of 26×26 μm). The entrance slit was set to 0.001 mm. Preliminary investigations in the wavelength range 200-1000 nm showed that N and O emission lines were dominant for the conditions of interest. Therefore, the analysis range was limited to 670-900 nm. The spectrum was calibrated in absolute intensity using a low power halogen source Avantes AvaLight-DHc. The wavelength calibration was performed using a low pressure mercury (Hg) lamp. The resolution was determined from the Hg lamp as well and it resulted in 0.1 nm Full Width Half Maximum (FWHM), which was not sufficient to resolve the single lines of the Oxygen triplet at 777 nm.

The PMT spectroscopy was applied to the plasma in the plenum chamber to investigate the temporal evolution of the emission signature. The optical fiber channel was used again to couple the light to the front entrance slit of the spectrograph (Fig. 2). A mirror was used inside the spectrograph to switch the diffracted light from the front exit (where the CCD camera was placed) to the side exit (where the PMT was placed). The grating was set to a central wavelength of 777 nm, to capture the temporal evolution of the light intensity associated to the O triplet. The spectral range was estimated to be about 20 nm. The entrance and exit slit were both set to 0.1 mm. The shutter was left open. The PMT was a Hamamatsu H7680 with a spectral range going from 400 nm to 900 nm and a bialkali photocathode. The gate/trigger signal to the PMT was provided through an Agilent 33120A 15 MHz waveform generator. Whereas, the output signal was acquired by means of an Agilent DSO6034A oscilloscope. The sampling frequency was set to 400 kHz and the acquisition interval to 2 s. The automatic control and acquisition were performed remotely using LabView.

The total pressure was measured using a Validyne P55A (0-22 bar range) connected to a pressure tap located on the optical access disk as well (Fig. 2). The mass-averaged total enthalpy (H_0) was measured applying a heat balance method, following the procedure outlined in [6] and [7]. In such method, H_0 is determined by dividing the total power input by the mass flow rate of the test gas. The total power input is the electrical power minus the Joule heating loss in the ballast resistors used for current regulation and the cooling water loss. The mass-averaged total enthalpy was also determined using an improved version of the ARCFLO code. Details about the code can be found in [8] and [9].

2.2. VKI Plasmatron

The VKI Plasmatron facility is the biggest and most powerful ICP torch worldwide. It uses a 1.2 MW RF power supply to ignite and sustain the plasma discharge. First of all, the 11 kV, 50 Hz voltage level coming from the network is adapted using a 1.7 MVA transformer (Fig. 3). The output signal is then rectified using a 12 pulses bridge and smoothed using chokes. The nominal values of DC voltage and current are 250 V and 5000 A respectively. A 1.2 MW, 400 kHz MOS inverter is then used to feed a single turn flat coil inductor. The RF cylindrical discharge is

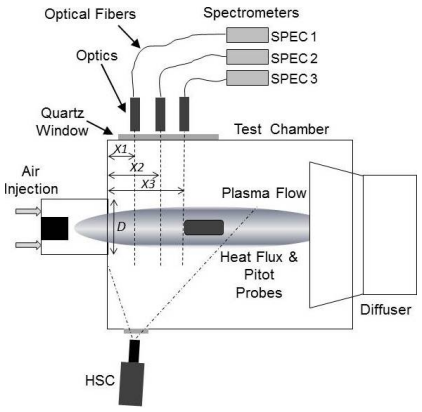

Figure 4: Simplified scheme of the experimental set-up for the VKI Plasmatron plasma wind tunnel. View from the top.

generated inside the torch composed of a quartz tube with an internal diameter of 200 mm and 5 mm thickness, and a cold-cage of D=160 mm internal diameter consisting of water-cooled copper segments inserted inside to prevent from severe overheating. The plasma discharge is ignited using a small amount of argon. The cold gas mixture (air at 16 g/s for the test conditions of interest) is then injected in an annular way into the quartz tube and heated up by Joule effect. The plasma enters the test chamber, where the test article is placed. In the case of interest no nozzle was installed (see Fig. 3) and the plasma jet was subsonic. The chamber is usually kept at a pressure between 15 mbar and 200 mbar, depending on the testing conditions. The plasma exits through a diffuser and it is cooled down by a water cooled heat exchanger. The vacuum system is composed by a roots pump and a set of three rotating vanes pumps. After proper dilution, the products are finally released to the atmosphere through an exhaust. The overall facility is equipped with a cooling system using a closed loop deionized water circuit coupled to fan coolers. See [4] and [5] for further details.

The experimental set-up is sketched in Fig. 4. The HSC imaging was performed using a Vision Research Phantom v7.0 CMOS camera (Fig. 4). The camera is characterized by a depth of 8 bit and the sensor is in black and white. The camera was equipped with a wide-angle VIS objective (12 mm focal length) to ensure the complete visualization of the plasma flow. The image resolution was set to 256×608 pixels and the acquisition rate was set to 13.16 kHz. The resulting acquisition interval was ~ 0.34 s for a total number of 4504 acquired frames.

Three Ocean Optics HR4000 spectrometers were looking at the plasma centerline for three different distances from the nozzle exit section: $x_1 = 19.5$ cm, $x_2 = 32$ cm and $x_3 = 44.5$ cm (1.2, 2 and 2.8 nozzle diameters D=160 mm respectively). The HR4000 spectrometer was characterized by a wavelength range of 200-1100 nm. The light was coupled to the spectrometer through a plano-convex fused silica lens and a quartz optical fiber (Ocean Optics QP600-SR/BX). The optical system was arranged according to the Newton's law for thin lenses to focus a collimated beam of light passing through the plasma centerline onto the fiber entrance. The beam of light had a diameter of ~ 2 cm, low enough to consider the emitted radiation at the three distances x_1, x_2 and x_3, uniform for the conditions of interest. The optical fibers were characterized by a 600 μm core diameter and an optimized numerical aperture to match the entrance slit of the spectrometer. The spectra were acquired using a 0.5 Hz repetition rate. The intensity calibration was performed in relative units combining a deuterium lamp in the UV (DH-2000 Mikropack) and a tungsten ribbon lamp in the VIS and NIR (OSRAM Wi 17/G). The wavelength calibration was performed using a low pressure Hg lamp (Oriel 6060). The Hg lamp was used to determine the spectral resolution as well and it resulted in ~ 0.9 nm FWHM. Each HSC movie was synchronized with the first spectrum acquired from the three spectrometers using a pulse generator.

The voltage output from the 12 pulses rectifier was monitored using a LeCroy LT584 oscilloscope at 100 kHz sampling frequency and 2 s acquisition interval. The oscilloscope was coupled with a calibrated 10× voltage probe. The heat flux (q_{cw}) was measured using a copper calorimeter embodied in a standard copper probe and the dynamic pressure (p_d) was measured by a Pitot probe [10]. Heat flux and pressure were the input for the VKI rebuilding code [11], which was used to retrieve the free stream temperature and enthalpy. Reference catalycity (γ_{ref}) and non-dimensional parameters were taken from [10]. Notice that both probes were injected 445 mm downstream the nozzle exit section, right at the location of the optical path at $x_3 = 445$ mm (see Fig. 4).

3. Elaboraton procedures

3.1. OES in the plenum chamber

The investigation of the thermodynamic state of the plasma flow produced by SCIROCCO is a challenging task. Due to the strong expansion through the

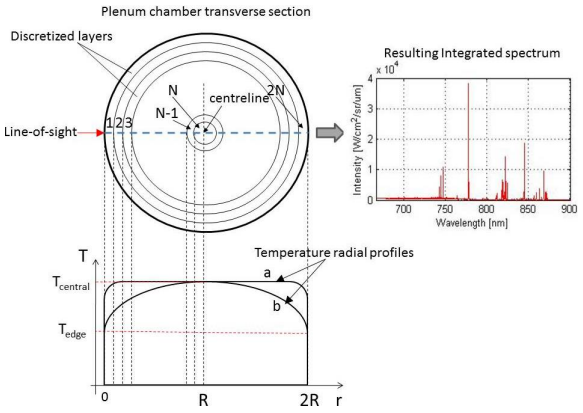

Figure 5: Simplified scheme of the procedure for the radial temperature profile extrapolation from line-of-sight measurements

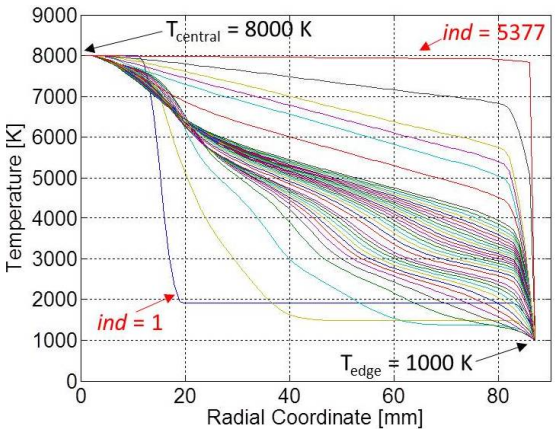

Figure 6: Example of radial temperature profiles extracted from ARCFLO. $T_{central}$ = 8000 K, T_{edge} = 1000 K

nozzle, the free-stream plasma is far from Local Thermodynamic Equilibrium (LTE) [12]. Therefore, the measurement of the total enthalpy using OES in free-stream is extremely difficult. However, before the plasma undergoes the compression-expansion phase (in the plenum chamber), it is still subsonic and the high P_0 (in the range 3.5 - 6.8 bar for the test cases of interest) promotes the thermalization of the energy level distributions according to the classical Boltzmann function. If the hypothesis holds true, the total enthalpy radial profile can be directly determined from the temperature profile. Furthermore, the mass averaged total enthalpy (i.e. one of the key parameters for ground testing) is known once temperature and velocity profiles are available. Of course, the LTE assumption is questionable. First of all, the effect of the electrical discharge located ~ 320 mm upstream the optical access disk in the cathode package could be non-negligible. Both the mere presence of the discharge and the arc root motion could promote non-equilibrium (NLTE). Moreover, there is the possibility that the thermodynamic conditions are non-uniform along the plenum chamber radius, as pointed out in [13]. Finally, the possibility of NLTE cannot be ruled out. Nevertheless, the elaboration procedure presented hereafter, which allowed to retrieve an estimation of the temperature and total enthalpy (h_0) profiles, is based on the assumption of LTE along the plenum chamber radial coordinate. The reliability of such assumption will be discussed together with the experimental results.

The chosen strategy consists of fitting the experimental calibrated spectrum with a theoretical spectrum, which is the result of the line-of-sight integration of simulated spectra according to a guessed parametric radial temperature profile. It is interesting to report that in similar works (such as [13]-[15]) the simplest approach was used regarding spectral emission: radial uniformity. A simplified scheme is presented in Fig. 5 to clarify the procedure. The transverse plane of the plenum chamber was discretized in $2N$=172 concentric disks. Because the plenum internal diameter is D_{pl}= 2 · R_{pl} =172 mm, the discretization step was 1 mm. The temperature profile was assumed axisymmetric with respect to the centerline. Furthermore, the thermodynamic features were assumed uniform within each single layer. The typical temperature radial profile shapes were extracted from ARCFLO and they were characterized by three parameters: central profile temperature i.e. temperature on the axis ($T_{central}$), temperature at the profile edges (T_{edge}) and a unique index associated to the particular shape of the profile (*ind*). In Fig. 5, two radial profiles are presented, just to show the difference between a fully developed profile (a) and a non-developed one (b). The developed profile corresponds to the uniform radial spectral emission case.

From Fig. 6 it is possible to appreciate a selection of temperature profiles (presented here for the sake of example) characterized by $T_{central}$ = 8000 K, T_{edge} = 1000 K and *ind* ranging from 1 to 5377. Indeed, the total number of profile shapes used for the spectral fittings was 5377. Index equal to 1 represents the case of starting profile, with the plasma condensed around the axis, where the electrical arc is located. Conversely, *ind* = 5377 represents the fully developed case and the example intermediate profiles represent the transition

between the two extremes. The set of 5377 profiles used for the fittings were considered representative of all the possible profiles the temperature can assume within the plenum chamber.

The spectral fitting was performed by minimizing the two parameters RMS error ($RMSE$) function, defined as in Eq. 1 [12]:

$$RMSE(T_{central}, ind) = \sqrt{\frac{\sum_{i=1}^{M}(S_{exp}(i) - S_{th}(i))^2}{M}}. \quad (1)$$

where M is the total number of spectral points, S_{exp} is the calibrated and normalized experimental spectrum and S_{th} is the normalized theoretical spectrum obtained from the integration of the theoretical spectra associated to each one of the discretized layers along the line-of-sight (see Fig.5), according to their own temperatures. T_{edge} was kept constant at 1000 K for the test cases of interest, following the approach outlined in [9]. The S_{th} which minimizes the the $RMSE$ function automatically gives back the resulting temperature radial profile. It is important to underline that the experimental calibrated spectrum is exactly the integrated light emission along the optical path. The theoretical spectra were obtained using the freeware Specair 2.2 [16] and the mole fractions for O and N species were obtained using the CEA code for LTE calculations [17].

A basic assumption of the aforementioned approach is that the optical fiber is collecting light along the optical path only, despite the fact that the numerical aperture is not 0 (i.e. 0.22 ± 0.02). However, between the plenum chamber wall surface and the fiber tip there is a 53 mm long cylindrical channel with opaque surfaces and 1.8 mm diameter. A test was performed using a VIS-NIR source coupled with the optical fiber, to ensure that the rays entering the hole with angles different from 0° did not reach the fiber acceptance cone. Conversely, the rays orthogonal to the plenum chamber internal surface were allowed to reach the fiber tip and to be guided to the spectrograph.

The radiation model took into account the NIR self-absorption [18]. The emission intensity at the $n-th$ discretized layer (refer to Fig. 5) and generic wavelength λ ($I_n(\lambda)$) was expressed as Eq. 2:

$$I_n(\lambda) = B_\lambda(T_n)[1 - exp(-k'_n(\lambda)L)] + I_{n-1}(\lambda)exp(-k'_n(\lambda)L). \quad n = 1, 2, ..., 2N. \quad (2)$$

where $B_\lambda(T_n)$ is the Planck blackbody function (depending on the temperature of the $n-th$ layer T_n), $k'_n(\lambda)$ is the absorption coefficient corrected for stimulated emission and L is the $n-th$ layer width (it was constant for the case of interest and equal to 1 mm). This is an iterative procedure: the emission from the $n-th$ layer depends on the emission from the layers between 0 and n-1. Additional details about the procedure can be found in [18].

3.2. PMT spectroscopy in the plenum chamber

The PMT spectroscopy was applied in the plenum chamber of the SCIROCCO facility to investigate the temporal evolution of the plasma flow optical emission. The time signal from the PMT was simply analyzed in the frequency domain applying a FFT transform [12]. Both arc root motion and power supply conversion ripple could induce unsteady heat and mass transfer in the flow, resulting in emission oscillations. In the first case, the random nature of the phenomenon will yield no specific spectral signature. Conversely, the 12 pulse rectifier introduces a frequency component at 600 Hz (the network frequency times the number of pulses: 50×12 Hz = 600 Hz) plus its harmonics. Additionally, the 50 Hz component itself (plus harmonics) could be found in the spectrum. The analysis of the FFT will tell how efficiently the capacitance filters and the high P_0 level in the plenum chamber damp the emission oscillations.

3.3. HSC imaging in free-stream

The investigation of the VIS optical emission field at high speed allowed to have a qualitative picture of the unsteady heat and mass transfer occurring in the plasma flow produced by VKI Plasmatron. The analysis of the acquired frames allowed to point out the effect of the test chamber pressure (p_{tc}) both in time and frequency domains [19]. Furthermore, the FFT analysis was applied to investigate the frequency components of the emission oscillations and a comparison was performed with the FFT of the voltage signal acquired by the oscilloscope at the output of the rectifier. The frequency analysis range was limited to 6.58 kHz (half of the acquisition rate 13.16 kHz, to fulfill the Nyquist criterion). However, it resulted sufficient to include the relevant frequency components for all the operating conditions of interest.

3.4. OES in free-stream

The temperature is one of the key physical quantities in plasma flow characterization and it is the starting point for the total enthalpy determination. The

peculiar features of the subsonic flow produced by the VKI Plasmatron facility make the task challenging. The unsteady heat and mass transfer induced by the RF power supply promotes intense mixing in the flow and a potential NLTE condition or a non-uniform thermodynamic state condition along the radial coordinate. Furthermore, the test chamber pressure and the power level could play a significant role in the definition of the boundary between LTE and NLTE conditions. The aforementioned issues were addressed by taking them from the other way around: the LTE assumption was taken for all the test cases of interest and the results were critically analyzed to check back the validity of the preliminary hypothesis.

The plasma flow temperature was measured by fitting the calibrated experimental spectra with theoretical spectra generated through Specair 2.2 [16] using the LTE approach. The best fit was obtained by minimizing the RMSE function defined in Eq. 1. In that case, S_{th} is the theoretical spectrum at the LTE temperature T_{LTE}. Of course, the RMSE is a function of T_{LTE} only in the present case. The attention was focused on the spectral region between 300 nm and 450 nm, where CN, N_2 and N_2+ mostly emit. The presence of the CN was due to carbonaceous impurities in the test gas. The mole fractions were generated using the VKI MUTATION library [20]-[22]. Preliminary investigations were performed including the self-absorption model offered by Specair 2.2 [16]. However, no significant difference was appreciated against the thin plasma case for the temperature range of interest.

Table 1: Test conditions matrix - CIRA SCIROCCO test campaign

Test	I	m_{air}	P_{el}	P_0	H_{0HB}	H_{0AF}
	A	kg s^{-1}	MW	bar	MJ kg^{-1}	MJ kg^{-1}
1	2014	0.70	14.8	3.5	11.6	11.63
2	2715	1.00	23.2	5.0	12.5	13.11
3	2806	1.30	27.0	6.3	11.7	13.00
4	2889	1.31	27.9	6.3	12.0	13.27
5	3801	1.29	36.0	6.8	14.1	15.50
6	3805	1.30	36.2	6.8	14.1	15.50
7	4024	0.84	31.3	4.7	16.6	17.08

An important aspect to be considered is that the presented experimental set-up only allowed to measure line-of-sight spectra at the plasma centerline. No deconvolution methods (such as Abel inversion) could be applied to retrieve the radial temperature profile. However, the two methodologies can be considered equivalent when the plasma is approximated by an uniform and homogeneous column. Therefore, if the temperature gradients along the radius are sufficiently low, while greatly simplifying the analysis procedure, the use of line-of-sight spectra would not produce any noticeable temperature difference with respect to the one obtained through de-convolution methods. To validate such hypothesis, the radial temperature profiles were obtained for one selected operating condition (P=200 kW and p_{tc}=100 mbar) at x_1 and x_3 distances. The spectra were acquired during a previous test campaign at the VKI Plasmatron and the temperature was retrieved by applying the same fitting procedure described in the present subsection. The maximum temperature difference found between the centerline and the plasma edges was $\sim$ 800 K ($\sim$ 10% of the centerline temperature), therefore the line-of-sight approach could be considered reliable. The detailed description of the experimental set-up and calibration process can be found in [23].

The second major issue is related to the unsteady nature of the plasma flow. The fluctuations in the plasma correspond to optical emission fluctuations and in turn to temperature fluctuations. Because of the spectrometers limited sampling frequency (i.e. 0.5 Hz), only stationary phenomena could be investigated. Indeed, the spectrometer acquires a spectrum which is the integration of all the spectral signatures emitted during the exposure time, according to the temperature evolution. Unfortunately, the integrated (i.e. averaged) spectrum does not correspond in general to the spectrum at the average plasma temperature. The distribution of the energy levels is influenced by the temperature of course, but it is not possible to establish any simple relation between the latter and the associated spectral signature. The issue will be further discussed in Section IV, along with the experimental results.

4. Experimental results

4.1. OES in the plenum chamber

The test campaign performed in the CIRA SCIROCCO facility consisted of seven operating conditions. The relevant parameters and the results from the fitting procedure are reported in Table 1. The test cases are listed for increasing values of arc current. The nominal conditions for test 5 and 6 were equal: the acquisitions were performed in the context of the same run within 2 minutes. That allowed to investigate the short term repeatability of the measurements.

P_{el} is the electrical power, H_{0HB} is the mass averaged total enthalpy obtained through heat balance method and H_{0AF} is the one from ARCFLO. The maximum measurement errors (combination of statistical,

Table 2: Results from fitting procedure - CIRA SCIROCCO test campaign

Test	$T_{central}$ K	$\Delta T_{central}$ K	ind -	Δind -	$RMS\,E_{min}$ -	$\Delta RMS\,E_{min}$ -	$h_0(r=0)$ MJ kg^{-1}	$\Delta h_0(r=0)$ MJ kg^{-1}
1	7780	117	5267	49	0.0125	1.7596e-4	29.6	1.45
2	7470	73	5336	15	0.0068	2.0172e-4	24.1	0.85
3	7590	134	5209	20	0.0065	1.1547e-4	24.4	1.54
4	7580	83	5235	31	0.0059	1.7650e-4	24.3	0.95
5	7820	75	5225	16	0.0068	2.0633e-4	26.6	0.87
6	7860	110	5202	12	0.0074	1.8974e-4	27.1	1.28
7	8360	88	5228	22	0.0164	1.9295e-4	34.6	1.06

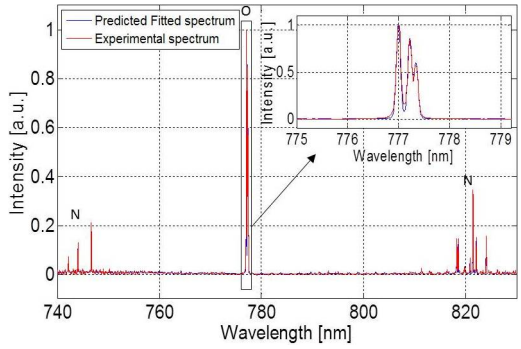

Figure 7: Fitting result for test 2 in the range 740-830 nm - CIRA SCIROCCO test campaign

instrumental and measurement chain errors) for the listed quantities were: ΔI = 100 A, Δm_{air} = 0.035 kg/s, ΔP_{el} = 21 kW, ΔP_0 = 0.11 bar and ΔH_{0HB} = 1.5 MJ/kg. It is extremely important to underline that the H_{0AF} is in the error band of H_{0HB} for all the test cases under investigation.

The spectral fitting was performed in the range 740 - 830 nm. The result from the spectral fitting for test 2 is reported in Fig. 7 as example. From the zoom, it is possible to observe the satisfactory fitting of the

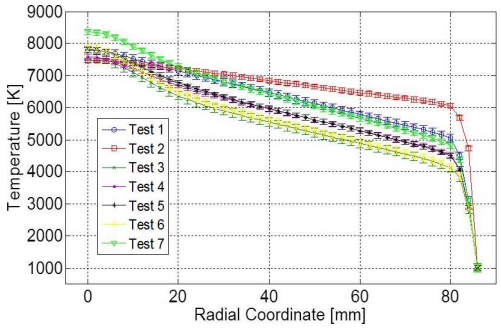

Figure 8: Temperature radial profiles in the plenum chamber - CIRA SCIROCCO test campaign

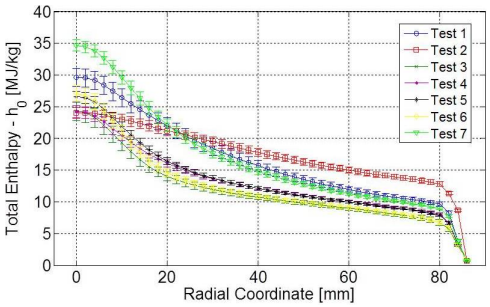

Figure 9: Total enthalpy radial profiles in the plenum chamber - CIRA SCIROCCO test campaign

oxygen triplet (although it is not completely resolved). The results of the fittings for the entire test matrix are reported in Table 2. $RMS\,E_{min}$ is the minimum of the RMSE function obtained from the fitting procedure, $h_0(r=0)$ is the total enthalpy at the centerline and it was determined from $T_{central}$ using CEA [17]. The measurement errors for $T_{central}$, ind and $RMS\,E_{min}$ (i.e. $\Delta T_{central}$, Δind and $\Delta RMS\,E_{min}$) were obtained in accordance to the procedure described in [12]. The sensitivity distribution [12] was computed for all the test cases. A unique absolute minimum was observed i.e. the fitting procedure results can be considered reliable.

The temperature radial profiles and the associated total enthalpy profiles for the test matrix are reported in Fig. 8 and Fig. 9 respectively. The profiles in test cases 5 and 6 were not in agreement within the error bar for the whole radius. Therefore, according to present results, temperature and total enthalpy were not fully repeatable in the short term.

Once the total enthalpy radial profile is known, it is possible to determine H_0 by applying Eq. 3 [24]:

$$H_0 = 1/m_{air} \cdot \int_0^{R_{pl}} 2\pi h_0(r)\rho(r)u_x(r)dr. \qquad (3)$$

where $\rho(r)$ is the plasma density in kg/m^3 and $u(r)$ is the velocity profile along the x axis in m/s (see Fig. 2). The plasma density profile was determined from CEA using the temperature profile as input. Conversely, the velocity profile could not be determined directly either from ARCFLO (it only provides the velocity in the arc column) or OES (because of the poor spectral resolution). Finally, H_0 cannot be determined from OES at the present stage.

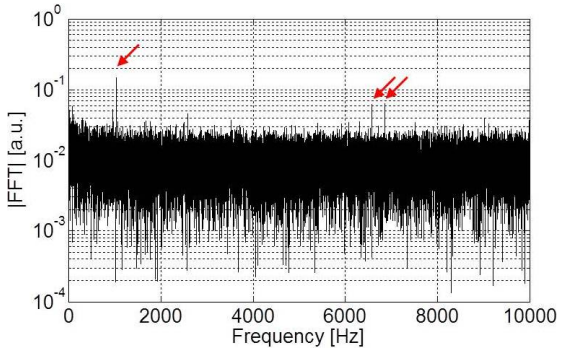

Figure 10: FFT modulus of the signal acquired from PMT - Test case 1

4.2. PMT spectroscopy in the plenum chamber

The PMT spectroscopy was applied only for test case 1 and 7 (the extremes) and the modulus of the FFT transform is presented in Fig. 10 for test case 1 as an example. The signal is normalized by the DC value and it is plotted only up to 10 kHz, because no relevant spectral features were observed for higher frequencies. The components indicated by the arrows were detected in the background signal as well (i.e. with plasma off): they were probably related to the electrical noise in the conditioning circuit. It is possible to observe that no 50 Hz or 600 Hz components (plus harmonics) were detected inside the plenum chamber (same conclusions for the test case 7), meaning that the capacitance filters damped them significantly. Furthermore, intensity was about ~ 2 order of magnitude lower than the DC for all the frequency components. Finally, the plasma can be considered temporally homogeneous within the plenum chamber and such conclusion is in accordance to the investigation performed in free-stream and reported in [25].

4.3. HSC imaging in free stream

The operating conditions and the results for the test campaign conducted in the VKI Plasmatron are summarized in Table 3. Heat flux (q_{cw}) and dynamic pressure (p_d) are included and their maximum measurement error is $\sim 10\%$. The mass flow rate was fixed to 16 g/s. The HSC imaging was applied to all the conditions and an example of normalized standard deviation (σ) distribution at 200 kW for the five pressure cases is reported in Fig. 11. At lower pressure (15 mbar) the emission oscillations were transported far in the flow. As the pressure rises, the oscillations were increasingly damped and most of the heat and mass transfer occurred close to the nozzle exit section. The distances at which the three spectrometers were looking at the plasma are indicated in Fig. 11 with dashed lines (lines 1, 2 and 3 correspond to x_1, x_2 and x_3 distances respectively). It is worth noting that, especially at 15 mbar, the spectrometer at x_1 was looking at a region with a significant fluctuations magnitude; i.e. the plasma could not be considered stationary in such region. In the subsection 4.4, the issue will be addressed. Furthermore, the mean radiation distribution (not presented here) showed that the plasma shrinks as the pressure rises. This resulted true for all the power settings. Although no analysis is presented here, the power level played a role as well: increasing the power, the heat and mass transfer was promoted. However, such effect was less marked than the one related to p_{tc}.

Table 3: Test conditions matrix and results - VKI Plasmatron test campaign

Test	P kW	p_{tc} mbar	m_{air} g s^{-1}	q_{cw} kW m^{-2}	P_d Pa	γ_{ref} -	$T(x_1)$ K	$T(x_2)$ K	$T(x_3)$ K	T_e K
1a	120	15	16	323.94	118.14	0.1	-	5986	-	3764
1b	160	15	16	559.40	143.59	0.1	6524	6270	5974	4902
1c	200	15	16	778.44	182.78	0.1	6709	6578	6454	5238
1d	250	15	16	1054.37	231.92	0.1	-	6868	6623	5538
1e	300	15	16	1346.71	264.47	0.1	-	-	-	5858
2a	120	50	16	216.15	22.66	0.1	-	-	-	3164
2b	160	50	16	594.22	37.51	0.1	6703	6454	6236	5135
2c	200	50	16	778.31	53.24	0.1	6980	6675	6477	5381
2d	250	50	16	1061.41	77.62	0.1	-	6907	6680	5652
2e	300	50	16	1582.33	95.05	0.1	-	-	-	6143
3a	120	100	16	134.73	9.63	0.01	-	-	-	2694
3b	160	100	16	384.14	13.92	0.01	6541	6388	5958	4714
3c	200	100	16	814.00	26.43	0.01	6853	6594	6465	5720
3d	250	100	16	-	-	-	7110	6959	6770	-
3e	300	100	16	-	-	-	-	7164	7041	-
4a	120	150	16	115.38	4.13	0.005	-	-	-	2911
4b	160	150	16	532.65	8.31	0.005	6490	6359	6108	5471
4c	200	150	16	844.09	14.80	0.005	6858	6576	6458	5933
4d	250	150	16	1175,44	29,04	0.005	6939	6792	6623	6190
4e	300	150	16	1704,80	42,29	0.005	7388	6908	6856	6761
5a	120	200	16	208.46	6.31	0.005	-	-	-	3342
5b	160	200	16	293.63	8.56	0.005	6500	6390	6290	3737
5c	200	200	16	859.58	13.58	0.005	6830	6628	6523	5910
5d	250	200	16	1195.20	20.94	0.005	7131	6940	6708	6241
5e	300	200	16	1696.01	37.20	0.005	7374	7198	7118	6623

The standard deviation represents a global quantity and does not allow to study the evolution of the different frequency components of the fluctuations. Therefore, the comparison between the modulus of the FFT (normalized with respect to the DC value) of the voltage signal and the FFT of the emission oscillations at x_1 was performed. The aim was to study the effect of the conversion ripple against the plasma emission oscillations. The comparison at 200 kW is presented in Fig. 12 for pressure cases 15, 100 and 200 mbar as example. The conversion ripple components (50 Hz plus harmonics and 600 Hz plus harmonics) were totally transmitted into the flow for the 15 mbar case and

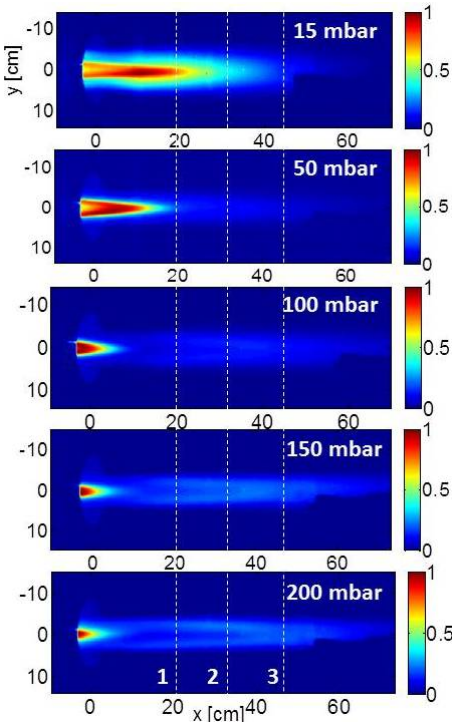

Figure 11: Standard Deviation distribution of the radiation oscillations for P=200 kW and m_{air}=16 g/s. Dashed lines 1,2 and 3 represent the distances x_1, x_2 and x_3.

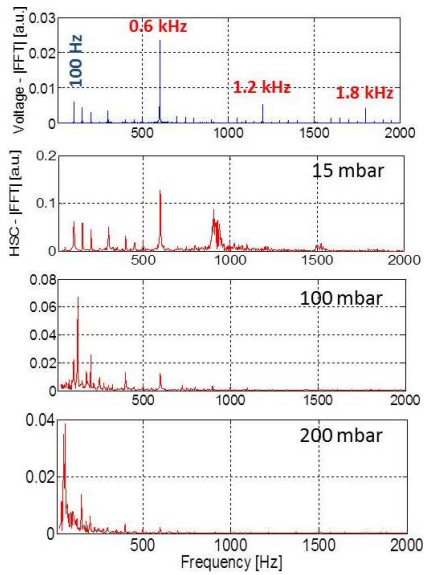

Figure 12: Comparison between voltage FFT and radiation oscillation FFT at x_1 for 15, 100 and 200 mbar cases. P = 200 kW

were clearly observable as emission radiation oscillations at x_1. The spectral content dramatically changed for higher pressures. The increase of pressure (i.e. inertia or matter) in the test chamber acted like a low pass filter with a decreasing cutoff frequency.

4.4. OES in free stream

The resulting temperatures at the positions x_1, x_2 and x_3 ($T(x_1)$, $T(x_2)$ and $T(x_3)$ respectively) are reported in Table 3 for all the test cases. The maximum error on the temperature was estimated to be $\sim$ 80 K. The free stream temperature (T_e) was rebuilt with the above mentioned VKI code [11] starting from the quantities in Table 3. It is important to underline that the probe was at 445 mm downstream the exit section of the nozzle, therefore T_e must be directly compared to $T(x_3)$.

An example of fitting result is presented in Fig. 13 for P= 200 kW and p_{tc}=100 mbar for the three spectrometers (test case 3c). The fitting was performed between 365 and 430 nm including the Δv=0 and -1 bands of the N_2+ first negative system and the Δv=0 band of the CN violet system. It is worth noting that the presence of the CN increased the fitting reliability: the relative weight between N_2+ first negative and CN violet Δv=0 bands is extremely sensitive to temperature. Figure 13 shows that the fitting quality was satisfactory for the three cases (and in general for all the test cases, although not presented here). However, it is important to underline that the quality increases with the pressure. It could be explained by a more efficient damping of the radiation oscillations at the spectrometers measuring point, inducing the plasma to go towards a stationary condition. Finally, the LTE assumption can be considered reasonable.

From Table 3, it is clear that no agreement exists between measured temperatures from OES and the ones from combined probe measurements and VKI rebuilding code. Such discrepancy is likely related to two main issues. The first one was the lack of knowledge regarding the γ_{ref} of the copper probes under different test conditions. Depending on the static pressure and power settings, T_e has a strong dependence on the value of γ_{ref} [10]. On the other hand, there was the effect of the radiation oscillations on the acquired spectra. As already mentioned, the experimental set-up allowed to record at a repetition rate (0.5 Hz) much lower than the typical frequency components of the plasma fluctuations. Therefore, the acquired spectra were in general not representative of the average temperature of the plasma flow. The resulting temperature from the fittings $T(x_3)$ could not directly compare to

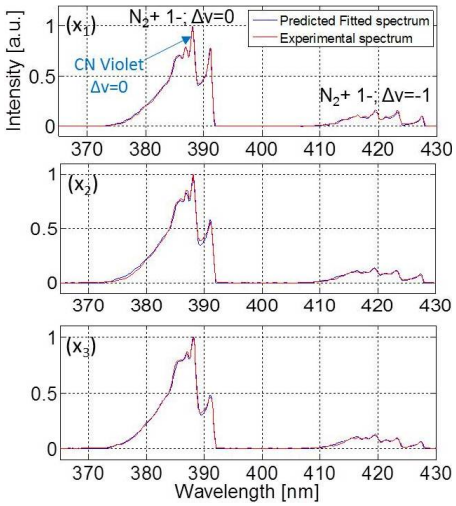

Figure 13: Spectral fitting results at x_1, x_2 and x_3 for P= 200 kW and p_{tc}=100 mbar

T_e, which was obtained by actual average measures of q_{cw} and p_d using the probes. Preliminary results from ongoing simulations (combining OES and HSC results) showed that the spectrometers could significantly overestimate the actual plasma temperature. In any case, the problem must be considered indeterminate at the present stage. The next step would be to use a time-resolved OES approach to capture the evolution of the spectral signature emitted from the plasma and measure the actual average temperature. Furthermore, such approach would allow to independently determine h_0 and the γ_{ref} of the copper probe for all the test conditions.

5. Conclusions

Optical emission diagnostics were applied for the flow characterization of the two major European plasma wind tunnels: CIRA SCIROCCO and VKI Plasmatron. The general aim of the work is to improve ground testing methodologies for Thermal Protection Systems (TPS) characterization. Seven operating conditions were tested in the SCIROCCO arc-jet facility, with a mass-averaged total enthalpy (H_0) ranging from 11.6 to 16.6 MJ/kg. H_0 was estimated using both a heat-balance method and an improved version of the ARCFLO simulation code. They resulted in agreement within error bars for all the test conditions. Furthermore, the radiation from the plenum chamber was analyzed using Optical Emission Spectroscopy (OES) and Photomultiplier (PMT) spectroscopy. Using an optical path reversal OES technique, the temperature and total enthalpy (h_0) radial profiles were obtained. The LTE assumption was adopted. Both profiles resulted non-uniform for all the test cases. Next step would be either to use simulations or absorption techniques, such as TDLAS (Tunable Laser Diode Absorption) or LIF (Laser Induced Fluorescence), to determine the velocity radial profile (u_x) in the plenum chamber. Knowing h_0 and u_x, it would be possible to determine H_0 by spectroscopy and finally validate both the optical path reversal technique and the LTE assumption against heat-balance method and ARCFLO results. The PMT spectroscopy was applied to the radiation from the plenum chamber as well. The attention was focused on the oxygen triplet (around 777 nm) and the repetition rate was 400 kHz. No significant frequency components were found in the spectrum, confirming the temporal homogeneity already pointed out for the free stream flow [25].

High Speed Camera (HSC) imaging and OES were applied to the free stream plasma produced by the VKI Plasmatron Inductive Coupled Plasma (ICP) torch. The operating conditions (25 in total) were characterized by an electrical power between 120 and 300 kW and a static pressure (p_{tc}) between 15 and 200 mbar. HSC imaging was used to point out the effect of the AC/DC ripple from the power supply on the plasma. The time domain analysis showed that p_{tc} is a driving parameter for the plasma instabilities. Furthermore, The FFT analysis showed that ripple components (50 and 600 Hz plus harmonics) were transported in the flow in different ways depending on the pressure. The facility acts like a low pass filter with cutoff frequency decreasing with increasing p_{tc}. Further investigations are ongoing. The spectra acquired from three positions along the centerline (1.2, 2 and 2.8 times the nozzle diameter D=160 mm) where used to measure the free-stream temperature. The LTE assumption was adopted and the fitting was performed on selected N_2+ first negative and CN violet bands. The quality of the fitting resulted satisfactory for the test cases, meaning that the LTE assumption can be considered reasonable. However, no agreement was found between OES and results obtained by combining heat flux and Pitot probe measurements with the VKI rebuilding code calculations [11]. The reason is likely due to both lack of knowledge regarding the reference catalycity (γ_{ref}) of the probes and the effect of the plasma oscillations on the spectral measurements. Due to the low repetition rate (0.5 Hz), the spectrometers were only able to acquire an integrated

spectrum over the radiation fluctuations occurring in the plasma. The resulting temperature could not be directly related to the average temperature obtained through the probe. The further step would be to use time-resolved spectroscopy techniques, such as intensified camera spectroscopy or TDLAS, to resolve the time evolution of the plasma temperature, determine h_0 and check back the γ_{ref} values.

Acknowledgments

The author would like to thank Campania Aerospace and CIRA for the Ph.D. grant; the VKI for the financial support during the Plasmatron test campaign; Bernd Helber and Francesco Panerai for their crucial contributions. Finally, thanks to both CIRA SCIROCCO and VKI Plasmatron groups.

References

[1] O. Chazot, R. Regnier and A. Garcia Munoz, Simulation Methodology in Plasmatron Facility and Hypersonic Wind Tunnels. Proceedings of the 12th International Conference on Method of Aerophysical Research, Novosibirsk, Russia, 2004. Published by "Nonparel", 2004, ISBN5-93089-005-6.

[2] G. Russo, F. De Filippis, S. Borrelli, M. Marini and S. Caristia, The SCIROCCO Plasma Wind Tunnel: a New Hypersonic Capability, Progress in Astronautics and Aeronautics 198 (2002) 315-351.

[3] S. Caristia, F. De Filippis, A. Del Vecchio and E. Graps, SCIROCCO PWT Facility for High Temperature Materials, Assembly Testing, Proceedings of 54th International Astronautical Congress, Bremen, Germany, 2003.

[4] B. Bottin, M. Carbonaro, S. Zemsch and G. Degrez, Aerothermodynamic Design of an Inductively Coupled Plasma Wind tunnel, no. AIAA 1997-2498, 32nd AIAA Thermophysics Conference, Atlanta, USA, 1997.

[5] B. Bottin, S. Paris, V. Van der Haegen and M. Carbonaro, Experimental and Computational Determination of the VKI Plasmatron Operating Envelope, no. AIAA 1999-3607, 30th AIAA Plasmadynamics and Lasers Conference, Norfolk, USA, 1999.

[6] C. Park, G. A. Raiche, II, D. M. Driver, J. Olejniczak, I. Terrazas-Salinas, T. M. Hightower and T. Sakai, Comparison of Enthalpy Determination Methods for Arc-Jet Facility, Journal of Thermophysics and Heat Transfer 20 (4) (2006) 672-679.

[7] T. M. Hightower, J. A. Balboni, C. L. Mac Donald, K. F. Anderson and E. R. Martinez, Enthalpy by Energy Balance for Aerodynamic Heating Facility at NASA Ames Research center Arc Jet Complex, Proceedings of 48th International Instrumentation Symposium, San Diego, CA, 2002.

[8] Aerotherm Corporation, ARCFLO Computer Code, Plasma Arc Heater Modeling, Aerotherm user manual 0713-93-011 (1993).

[9] K. H. Kim, O. H. Rho and C. Park, Navier-Stokes Computation of Flows in arc Heaters, Journal of Thermophysics and Heat Transfer, 14 (2) (2000) 250-258.

[10] F. Panerai, Aerothermochemistry Characterization of Thermal Protection Systems, PhD Thesis, von Karman Institute for Fluid Dynamics & University of Perugia (2011) (to be published).

[11] P. Barbante, G. Degrez, and G. S. R. Sarma, Computation of Nonequilibrium High Temperature Axisymmetric Boundary-layer Flows, Journal of Thermophysics and Heat Transfer, 16 (4) (2002) 490-497.

[12] A. Cipullo, L. Savino, E. Marenna and F. De Filippis, Thermodynamic State Investigation of the Hypersonic Air Plasma Flow Produced by the Arc-et Facility SCIROCCO, Aerospace Science and Technology (2011) (to be published. Available on line)

[13] D.G. Fletcher, Nonintrusive Diagnostic Strategies for Arcjet Stream Characterization, RTO AVT Course on Measurement Techniques for High Enthalpy and Plasma Flows, Rhode-Saint-Genese, Belgium, 1999 (published in RTO EN-8).

[14] M. A. Rob, L. H. Mack, S. Arepalli and C. D. Scott, Characterization of Plenum Spectra in an Arcjet Wind Tunnel, no. AIAA 95-2126, 30th AIAA Thermophysics Conference, San Diego, CA, 1995.

[15] J. M. Donohue, D. G. Fletcher and C. S. Park, Emission Spectral Measurements in the Plenum Chamber of an Arcjet Wind Tunnel, no. AIAA 98-2946, 7th AIAA/ASME Joint Thermophysics and Heat Transfer Conference, Albuquerque, NM, 1998.

[16] C. O. Laux, Radiation and Nonequilibrium Collisional-radiative Models. Physicochemical Modeling of High Enthalpy and Plasma Flows, von Karman Institute Lecture Series 2002-07, D. G. Fletcher, J.-M. Charbonnier, G. S. R. Sarma, T. Magin (Eds.), Rhode-Saint-Genese, Belgium (2002).

[17] B. J. McBride and S. Gordon, Computer Program for Calculation of Complex Chemical Equilibrium Compositions and Applications, NASA Users manual (1996).

[18] C. O. Laux, Optical diagnostics and radiative emission of air plasmas, Ph.D. thesis, Stanford University (1993).

[19] I. Benito, M. Aleo and Y. Babou, VKI Plasmatron Performances Investigations: I. Air Plasma Jet Time Dependant Behaviour, no. ESA SP-667, Proceedings of the 3rd International Workshop on Radiation of High Temperature Gases in Atmospheric Entry, Heraklion, Greece, 2008.

[20] T. E. Magin, A Model for Inductive Plasma Wind Tunnels, Ph.D. thesis, von Karman Institute for Fluid Dynamics, Belgium (2004).

[21] A. Munafo, M. Panesi, R. Jaffe, A. Lani and T. Magin, Vibrational State to State Kinetics in Expanding and Compressing Nitrogen Flows, no. AIAA 2010-4335, 10th AIAA/ASME Joint Thermophysics and Heat Transfer Conference, Chicago, IL, 2010.

[22] M. Panesi, Physical Models for Nonequilibrium Plasma Flow Simulations at High Speed Re-entry Conditions, Ph.D. thesis, von Karman Institute for Fluid Dynamics (2009).

[23] A. Cipullo, Plasma Flow Characterization by means of Optical Emission Diagnostics, Research Master project report, von Karman Institute for Fluid Dynamics (2010).

[24] A. B. Witte, Part I. Experimental Investigation of an Arc-Heated Supersonic Free Jet; Part Ii. Analysis of One-Dimensional Isentropic Flow for Partially Ionized Argon, Ph.D. Thesis, California Institute of Technology (1967).

[25] A. Cipullo, L. Savino, E. Graps, C. Purpura, L. Zeni and F. De Filippis, Investigation of Spatial and Temporal Flow Homogeneity in Arc-jet Plasmas using Intrusive and Non-intrusive Diagnostics, no. ESA SP-692, Proceedings of the 7th European Symposium on Aerothermodynamics for Space Vehicles, Bruges, Belgium, 2011.